

Article

# Pt/CeMnO<sub>x</sub>/Diatomite: A Highly Active Catalyst for the Oxidative Removal of Toluene and Ethyl Acetate

Linlin Li, Yuxi Liu \*, Jiguang Deng, Lin Jing, Zhiquan Hou, Ruyi Gao and Hongxing Dai \* 

Beijing Key Laboratory for Green Catalysis and Separation, Key Laboratory of Beijing on Regional Air Pollution Control, Key Laboratory of Advanced Functional Materials, Education Ministry of China, Laboratory of Catalysis Chemistry and Nanoscience, Department of Chemical Engineering, Faculty of Environment and Life, Beijing University of Technology, Beijing 100124, China

\* Correspondence: yxliu@bjut.edu.cn (Y.L.); hxdai@bjut.edu.cn (H.D.); Tel.: +86-10-(67)396118 (H.D.); Fax: +86-10-(67)-391983 (H.D.)

**Abstract:** Pt nanoparticles and a CeMnO<sub>x</sub> composite were loaded on the surface of the natural diatomite material to generate the Pt/CeMnO<sub>x</sub>/diatomite using the redox precipitation and impregnation methods. The physicochemical properties of the catalysts were characterized by means of various techniques. The catalytic properties and resistance to H<sub>2</sub>O and SO<sub>2</sub> of the catalysts were measured for the oxidation of typical volatile organic compounds (i.e., toluene and ethyl acetate). Among all of the as-prepared samples, Pt/CeMnO<sub>x</sub>/diatomite exhibited the highest catalytic activity: the temperatures ( $T_{90\%}$ ) at a toluene or ethyl acetate conversion of 90% were 230 and 210 °C at a space velocity (SV) of 20,000 mL g<sup>-1</sup> h<sup>-1</sup>, respectively, and the turnover frequency (TOF<sub>Pt</sub>) at 220 °C was 1.04 μmol/(g<sub>cat</sub> s) for ethyl acetate oxidation and 1.56 μmol/(g<sub>cat</sub> s) for toluene oxidation. In particular, this sample showed a superior catalytic activity for ethyl acetate oxidation at low temperatures, with its  $T_{50\%}$  being 185 °C at SV = 20,000 mL g<sup>-1</sup> h<sup>-1</sup>. In addition, the Pt/CeMnO<sub>x</sub>/diatomite sample possessed good sulfur dioxide resistance during the toluene oxidation process. In the presence of SO<sub>2</sub>, some of the SO<sub>2</sub> molecules were adsorbed on diatomite, which protected the active sites from being poisoned by SO<sub>2</sub> to a certain extent. The pathways of ethyl acetate and toluene oxidation over Pt/CeMnO<sub>x</sub>/diatomite or Pt/CeMnO<sub>x</sub> were as follows: The C–C and C–O bonds in ethyl acetate are first broken to form the CH<sub>3</sub>CH<sub>2</sub>O\* and CH<sub>3</sub>CO\* species or toluene is first oxidized to benzaldehyde and benzoic acid, and all of these intermediates are then converted to CO<sub>2</sub> and H<sub>2</sub>O. This work can provide a strategy to develop efficient catalysts with high catalytic activity, durability, low cost, and easy availability under actual working conditions.

**Keywords:** Ce–Mn composite oxide; supported platinum catalyst; volatile organic compound; ethyl acetate oxidation; toluene oxidation; sulfur dioxide resistance



**Citation:** Li, L.; Liu, Y.; Deng, J.; Jing, L.; Hou, Z.; Gao, R.; Dai, H. Pt/CeMnO<sub>x</sub>/Diatomite: A Highly Active Catalyst for the Oxidative Removal of Toluene and Ethyl Acetate. *Catalysts* **2023**, *13*, 676. <https://doi.org/10.3390/catal13040676>

Academic Editors: Eduardo Miró, Ezequiel David Banus and Juan Pablo Bortolozzi

Received: 18 February 2023

Revised: 24 March 2023

Accepted: 27 March 2023

Published: 30 March 2023



**Copyright:** © 2023 by the authors. Licensee MDPI, Basel, Switzerland. This article is an open access article distributed under the terms and conditions of the Creative Commons Attribution (CC BY) license (<https://creativecommons.org/licenses/by/4.0/>).

## 1. Introduction

Volatile organic compounds (VOCs) include a wide range of compounds, such as oxygenates, light hydrocarbons, aromatic hydrocarbons, and halogenated hydrocarbons. Most of the VOCs emitted from industries are harmful to public health and the atmosphere environment [1]. Among all the elimination methods, catalytic oxidation has been regarded as one of the most promising technologies to eliminate VOC emissions because of its high efficiency, low cost, and lower secondary pollution [2].

Transition-metal oxides or supported noble metal catalysts are active for the abatement of VOCs, among which supported noble metal catalysts have attracted much attention due to their excellent low-temperature catalytic activities and good resistance to poisoning. For instance, Zhang et al. [3] reported that the atomically dispersed Pt/MnO<sub>2</sub> catalyst showed a complete conversion of toluene to CO<sub>2</sub> at a temperature of 220 °C and a space velocity of 48,000 mL g<sup>-1</sup> h<sup>-1</sup>. Although this type of catalyst exhibits excellent performance,

its industrial application is greatly restricted due to its high cost. Usually, introducing the transition-metal oxides as the promoter can construct dual or even multiple active sites, thus enhancing the performance of the catalyst [4]. Recently, many researchers have focused on the development of metal oxide catalysts (e.g.,  $\text{MnO}_x$ ,  $\text{Co}_3\text{O}_4$ , and  $\text{CeO}_2$ ) owing to their low cost, high thermal stability, and good oxygen storage capacity. Because of these outstanding characteristics, these types of catalysts have been widely used in VOC removal, especially for the elimination of oxygenated compounds. Lu et al. [5] prepared the  $\text{ZrO}_2$ -supported Cu-Mn-Ce mixed oxide catalysts by an impregnation method and found that this catalyst possessed a good thermal stability even after calcination at 900 °C, and the formation of a  $\text{Zr}_{0.88}\text{Ce}_{0.12}\text{O}_2$  phase could improve the activity and thermal stability of the catalyst.

The choice of a support is another important factor affecting the catalytic performance of the supported catalyst. Diatomite is an amorphous silica material that consists of silicon dioxide ( $\text{SiO}_2$ ) along with small quantities of impurities, such as Al, Fe, Ca, Mg, etc. Diatomite has a porous structure, low density, and large specific surface area, and it is usually used as a support to disperse the active species [6–9]. For example, Wang et al. [10] used V-doped  $\text{TiO}_2$ /diatomite as a photocatalyst for the degradation of rhodamine B. Nevertheless, there have been few reports on the use of diatomite as a catalyst for thermocatalysis. The surface of diatomite is negatively charged after hydrolysis, which inhibits the electrostatic adsorption and chemisorption of reactant molecules. Therefore, it is essential to modify the surface of diatomite to improve its adsorption activity. If diatomite is used as support to load the mixed transition-metal oxides and noble metals, one can expect to obtain efficient catalysts for the catalytic oxidation of VOCs. For instance, Zhou et al. [11] pointed out that the  $\text{CeO}_2$ -modified diatomite with the anchoring of single Pt atoms showed a remarkable catalytic performance in the selective hydrogenation of phenylacetylene. Liu et al. [12] reported on  $\text{TiO}_2$ @diatomite catalysts with various  $\text{TiO}_2$  loadings using a facile solvothermal method with anhydrous ethanol as solvent for the removal of VOCs. The results indicated that, after introducing diatomite,  $\text{TiO}_2$  nanoparticles were mostly square-like in morphology and uniformly immobilized on the diatomite surface. The  $\text{TiO}_2$ @diatomite catalysts could effectively catalyze the removal of acetone and benzene, demonstrating their potential market applications and practical significance.

In the past few years, most of the research works have mainly focused on the catalytic removal of single components of VOCs. Under the actual operating conditions, however, most of the VOCs are present in the emissions as a mixture, and there have so far been no sufficient efforts to concurrently eliminate multicomponent VOCs. It is known that the oxidation of a VOC in a mixture differs from its single-component oxidation due to interactions of the different species with the catalyst. The mixture effect is tough to predict as either an inhibitive effect or a promotional effect and can be observed when the components of the VOC mixture are oxidized. Hence, it is necessary to assess the performance of catalysts for the removal of a multicomponent VOC mixture. For example, Lee et al. [13] prepared a 1 wt% Pt/ $\text{TiO}_2$  catalyst after a reduction pretreatment and observed that the tricomponent VOC mixture (formaldehyde, acetaldehyde, and toluene) was completely converted over this catalyst at a temperature of 200 °C and a space velocity of 24,000  $\text{mL g}^{-1} \text{h}^{-1}$ . Santos et al. [14] reported the effects of a VOC mixture on the activity and selectivity of the catalysts. It was observed that toluene inhibited both ethyl acetate and ethanol oxidation, which was more evident in ethyl acetate oxidation. The temperature for the complete conversion of ethyl acetate was about 210 °C when ethyl acetate was oxidized alone, but it was 250 °C or higher when ethyl acetate was oxidized in its mixture with toluene.

Considering the catalytic efficiency, anti-toxicity, and cost of the catalysts in actual industrial production, the  $\text{CeMnO}_x$  composite was selected as the second active component to be dispersed on the surface of diatomite, together with the Pt nanoparticles also being dispersed on the surface of  $\text{CeMnO}_x$ /diatomite. Hence, it was expected that the Pt/ $\text{CeMnO}_x$ /diatomite catalyst would exhibit excellent activity and good sulfur dioxide

resistance in the oxidation of toluene and ethyl acetate. The physical and chemical properties of Pt/CeMnO<sub>x</sub>/diatomite were determined by means of various characterization techniques. Furthermore, the catalytic oxidation of toluene and ethyl acetate as model reactions was employed to evaluate the catalytic activities of these materials. Industrial flue gas often contains certain concentrations of SO<sub>2</sub> and H<sub>2</sub>O, which requires the catalysts to show a good tolerance to sulfur dioxide and moisture. Thus, we need to investigate the performance of the typical catalyst for the oxidation of VOCs in the presence of SO<sub>2</sub> or H<sub>2</sub>O. Furthermore, Mn, Ce, and diatomite are cheap, easy to obtain, and environmentally friendly, and such formulated catalysts are of significance for industrial applications.

## 2. Results and Discussion

### 2.1. Crystal Phase Analysis

In order to clarify the crystal phase compositions of the samples, XRD and Raman characterization was made. The XRD results obtained by Figure 1A revealed that the composite oxides displayed obvious diffraction peaks of CeO<sub>2</sub> at  $2\theta = 29.0^\circ$ ,  $33.6^\circ$ ,  $48.2^\circ$ , and  $57.0^\circ$ , indicating that the CeO<sub>2</sub> in the samples was of a fluorite-type cubic structure. The crystal phase of the Pt/CeMnO<sub>x</sub>/diatomite sample can be more clearly seen from Figure 1B. Two peaks at  $2\theta = 21.8^\circ$  and  $31.9^\circ$  belonged to the amorphous SiO<sub>2</sub> in diatomite (JCPDS PDF# 39-1425). Compared with the peak positions of the published XRD pattern of CeO<sub>2</sub> ( $2\theta = 28.549^\circ$ ,  $33.077^\circ$ ,  $47.483^\circ$ , and  $56.342^\circ$ ) (JCPDS PDF# 34-0394), those of the as-obtained samples were slightly shifted to larger diffraction angles. Combined with no detection of the characteristic peaks of MnO<sub>2</sub>, it can be concluded that manganese ions enter the lattice of ceria to form a Ce–Mn-based solid solution or the MnO<sub>x</sub> is highly dispersed on the surface of CeO<sub>2</sub>. The possible reason for the slight shift in peak position was the incorporation of Mn ions to the lattice of CeO<sub>2</sub>, which made the lattice of ceria shrink ( $r_{\text{Mn}^{4+}} = 0.53 \text{ \AA}$ ,  $r_{\text{Mn}^{3+}} = 0.64 \text{ \AA}$ , and  $r_{\text{Ce}^{4+}} = 0.97 \text{ \AA}$ ) [15]. In addition, the formation of a Ce–Mn solid solution was also proven by the changes in peak intensity and shape. The wide diffraction peaks, the decreased intensity, and the disappeared characteristic peaks were also evidence for the formation of a Ce–Mn solid solution. The formation of such a Ce–Mn solid solution increased oxygen vacancies [16,17], which was beneficial for the improvement in catalytic performance.

The Raman spectra of the samples were further recorded to examine their structural information. Figure 1C shows Raman spectra of the MnO<sub>2</sub>, CeO<sub>2</sub>, CeMnO<sub>x</sub>/diatomite, and Pt/CeMnO<sub>x</sub>/diatomite samples. As observed for the pure MnO<sub>2</sub> sample, there were three bands at 180, 330, and  $636 \text{ cm}^{-1}$  [18]. For the pure CeO<sub>2</sub> sample, there was an intense band at  $462 \text{ cm}^{-1}$ . With the formation of the CeMnO<sub>x</sub> solid solution, the band in the pure CeO<sub>2</sub> sample was shifted from 462 to  $448 \text{ cm}^{-1}$ , implying the occurrence of lattice defects formed due to the incorporation of Mn ions into the CeO<sub>2</sub> lattice and partial replacement of Ce ions by Mn ions. Compared with the pure CeO<sub>2</sub> or MnO<sub>2</sub> sample, the broadening and weakening of Raman bands indicate the formation of lattice defects. These results were consistent with the XRD results, further confirming the formation of a Ce–Mn solid solution.

### 2.2. Morphology

The surface morphologies of the as-prepared samples were characterized by the SEM technique. As can be seen from Figure 2, the raw diatomite possessed a disk-like morphology with a smooth surface, uniform ordered pore structures, and well-aligned channels. The diameters of the pores and disk were 20–40 nm and 8–10  $\mu\text{m}$ , respectively. As shown in Figure 2c,d, the CeMnO<sub>x</sub> composite contained spherical and rod-like particles. After the CeMnO<sub>x</sub> was loaded on the surface of diatomite, the as-obtained sample was composed of disc-shaped diatomite and irregular CeMnO<sub>x</sub> particles, and the CeMnO<sub>x</sub> composite became more scattered on the diatomite surface (Figure 2e). The elemental mappings reveal that the Ce and Mn in CeMnO<sub>x</sub> were uniformly dispersed on the surface of diatomite (Figure 2f–i).

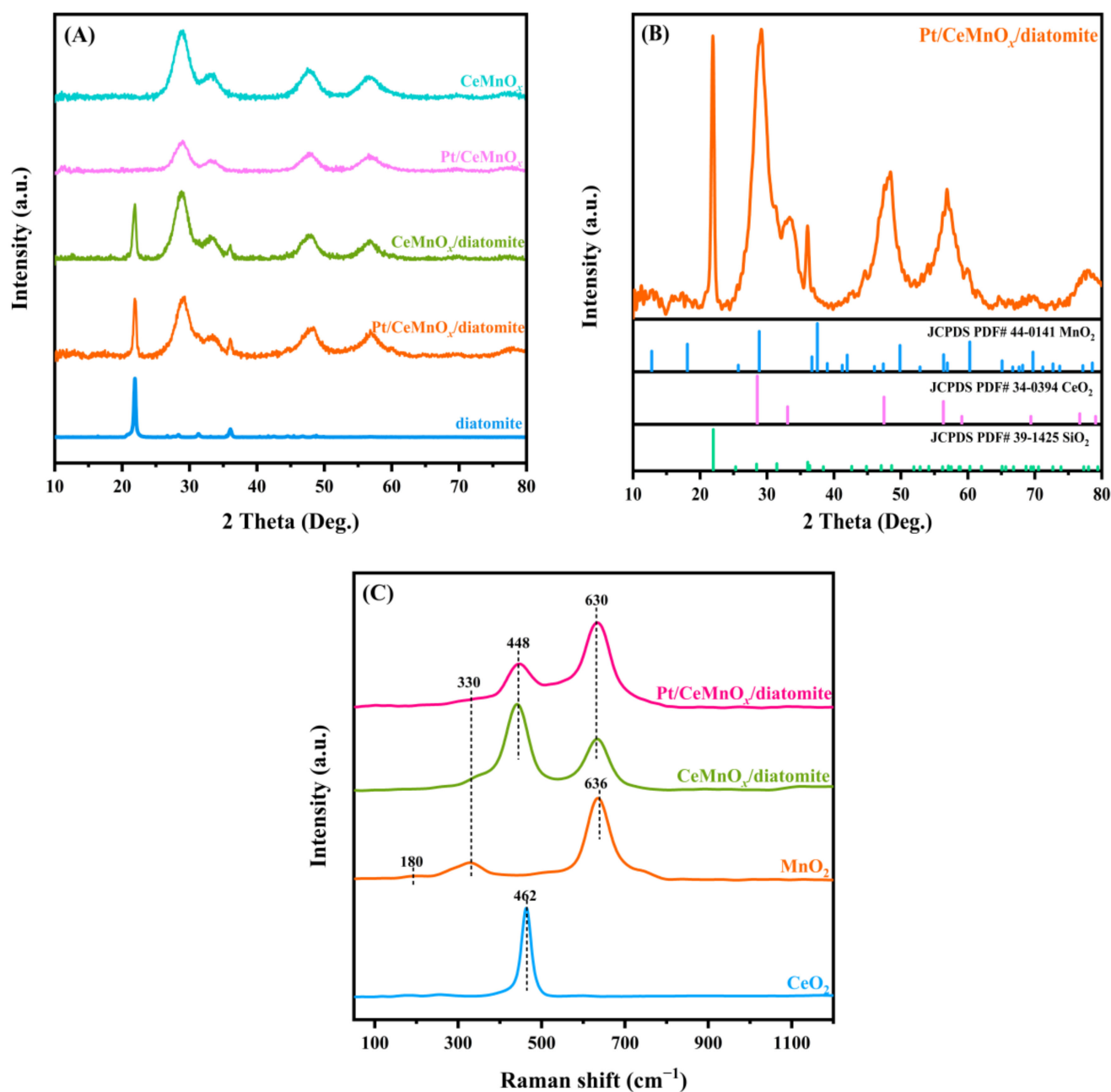


**Figure 1.** (A,B) XRD patterns and (C) Raman spectra of the samples.

### 2.3. Textural and Surface Properties

Surface areas, pore volumes, and pore-size distributions of the samples were analyzed using the BET technique, and their results are presented in Figure 3 and Table 1. The surface areas of the pure diatomite, CeMnO<sub>x</sub>, CeMnO<sub>x</sub>/diatomite, and Pt/CeMnO<sub>x</sub>/diatomite samples were 24.3, 128.2, 113.7, and 51.7 m<sup>2</sup>/g, respectively. From the pore diameter distributions and SEM images, it can be seen that the diatomite is a porous material with a disc-like morphology. The diatomite, CeMnO<sub>x</sub>, and CeMnO<sub>x</sub>/diatomite samples showed a type-IV isotherm. After the loading of CeMnO<sub>x</sub>, the surface areas and pore volumes of the as-obtained samples increased. However, there was no change in the pore size of the samples after the loading of CeMnO<sub>x</sub>. The surface area of Pt/CeMnO<sub>x</sub>/diatomite decreased with the loading of Pt nanoparticles, which was due to the deposition of Pt nanoparticles on the pores of diatomite.

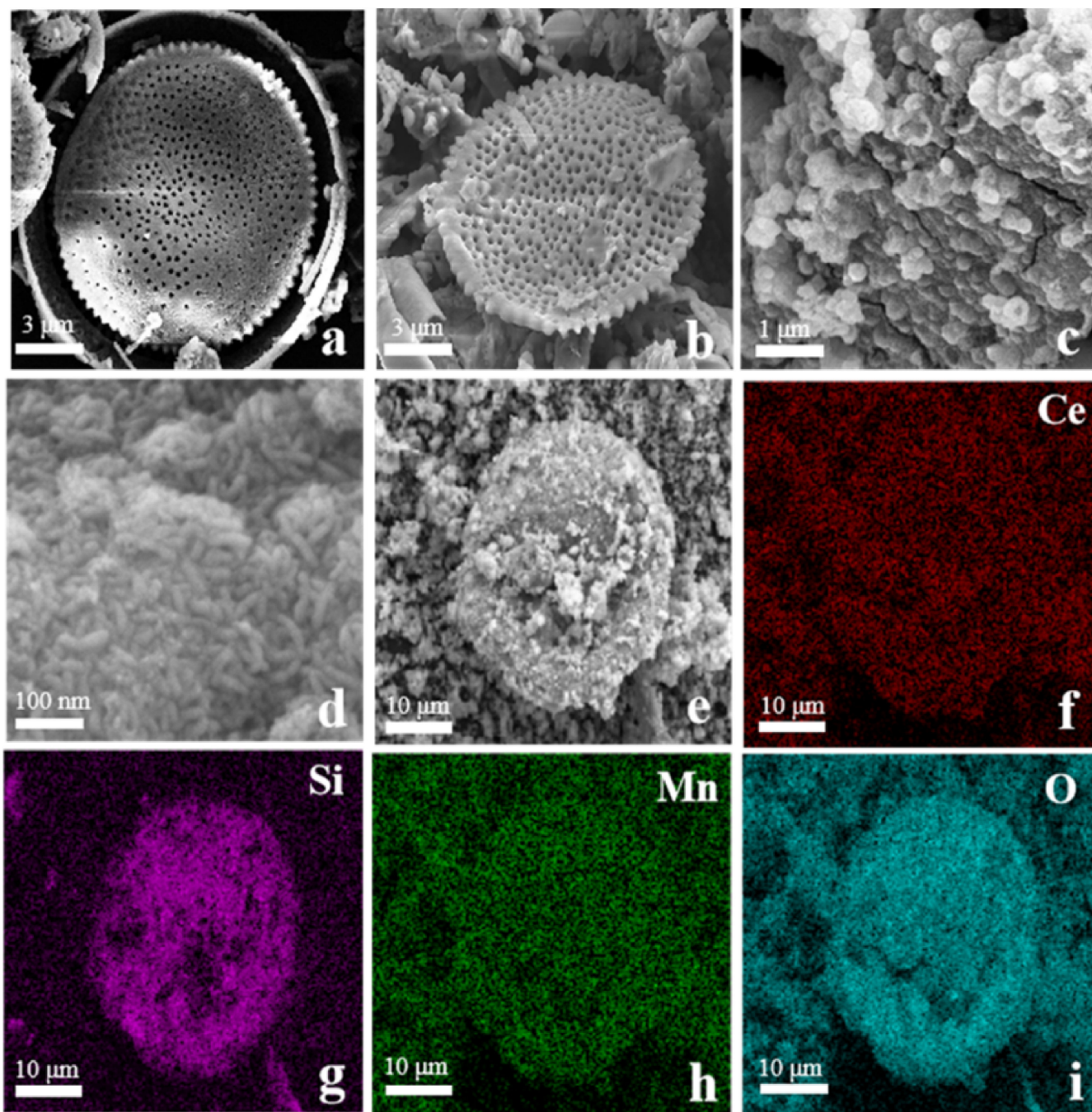


**Figure 2.** SEM images of (a,b) diatomite, (c,d)  $\text{CeMnO}_x$ , (e)  $\text{CeMnO}_x$ /diatomite, and (f–i) elemental mappings of  $\text{CeMnO}_x$ /diatomite.

**Table 1.** BET surface areas ( $S_{\text{BET}}$ ), pore volumes ( $V_{\text{pore}}$ ), and pore diameters ( $d_{\text{pore}}$ ) of the samples.

Sample	$S_{\text{BET}}$ ( $\text{m}^2/\text{g}$ )	$V_{\text{pore}}$ ( $\text{cm}^3/\text{g}$ )	$d_{\text{pore}}$ (nm)
diatomite	24.3	0.17	11.7
$\text{CeMnO}_x$	128.2	0.35	10.9
$\text{CeMnO}_x$ /diatomite	113.7	0.33	11.8
Pt/ $\text{CeMnO}_x$ /diatomite	51.7	0.31	24.1

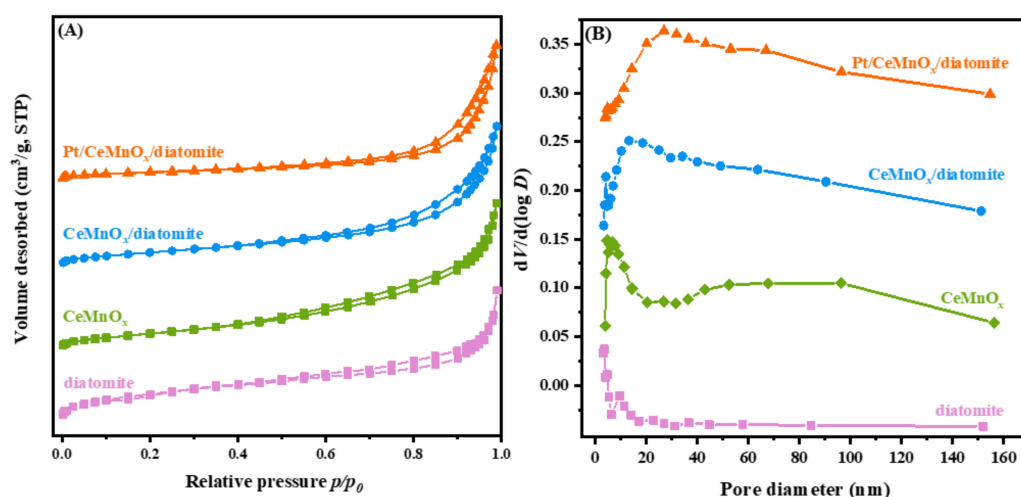


**Figure 3.** (A) Nitrogen adsorption–desorption isotherms and (B) pore-size distributions of the samples.

XPS experiments were carried out to analyze the surface element compositions, metal oxidation states, and oxygen species of the as-prepared samples. The obtained XPS spectra of O 1s, Ce 3d, Mn 2p, and Pt 4f are shown in Figure 4.

The corresponding surface element compositions are listed in Table 2.

**Table 2.** Surface element compositions and hydrogen consumption of the CeMnO<sub>x</sub>, CeMnO<sub>x</sub>/diatomite, Pt/CeMnO<sub>x</sub>, and Pt/CeMnO<sub>x</sub>/diatomite samples.

Sample	Surface Element Composition (mol/mol)				H <sub>2</sub> Consumption (mmol/g <sub>cat</sub> )
	Pt <sup>δ+</sup> /Pt <sup>0</sup> a Molar Ratio	(Mn <sup>2+</sup> + Mn <sup>3+</sup> )/Mn <sup>4+</sup> Molar Ratio	Ce <sup>3+</sup> /Ce <sup>δ+</sup> b Molar Ratio	O <sub>ads</sub> /O <sub>latt</sub> Molar Ratio	
CeMnO <sub>x</sub>	–	–	–	–	2.63
CeMnO <sub>x</sub> /diatomite	–	–	–	–	2.78
Pt/CeMnO <sub>x</sub>	2.91	2.27	0.09	0.21	2.67
Pt/CeMnO <sub>x</sub> /diatomite	4.23	3.83	0.1	0.29	2.97

a Pt<sup>δ+</sup> = Pt<sup>0</sup> + Pt<sup>2+</sup> + Pt<sup>4+</sup>; b Ce<sup>δ+</sup> = Ce<sup>4+</sup> + Ce<sup>3+</sup>.

As can be seen from Figure 4A, the O 1s spectrum with binding energy (BE), located at 529.1–531.9 eV, contained three components that could be ascribed to the surface lattice oxygen (O<sub>latt</sub>), adsorbed oxygen (O<sub>ads</sub>), and adsorbed molecular water (O<sub>H<sub>2</sub>O</sub>) or carbonate species [19], respectively. The O<sub>ads</sub>/O<sub>latt</sub> molar ratios on Pt/CeMnO<sub>x</sub> and Pt/CeMnO<sub>x</sub>/diatomite were 0.21 and 0.29 (Table 2), respectively, which were obtained by quantitative analysis of the O 1s peaks. The asymmetrical Mn 2p<sub>3/2</sub> signal of each sample was composed of three components at BE = 640.1, 641.7, and 644.1 eV (Figure 4B), which could be attributed to the surface Mn<sup>2+</sup>, Mn<sup>3+</sup>, and Mn<sup>4+</sup> species [20–22], respectively. It can be seen from Figure 4C that the Ce 3d orbits were divided into two groups of multi-peaks denoted as U and V. The V' and U' with BE = 895.6 and 904.34 eV were attributed to the Ce<sup>3+</sup> species on the sample surface. As shown in Figure 4D, the Pt 4f XPS spectrum of each sample consisted of six components at BE = 71.6 and 74.7, 72.8 and 76.1, and 74.1 and 77.7 eV, which were assigned to the Pt<sup>0</sup> [23], Pt<sup>2+</sup> [24], and Pt<sup>4+</sup> [25] on the surface of the sample.

The XPS results indicate that the molar ratio of O<sub>ads</sub>/O<sub>latt</sub> increased due to the addition of diatomite, i.e., enhancing the ability to activate the oxygen molecules of the sample. In addition, the molar ratio of (Mn<sup>2+</sup> + Mn<sup>3+</sup>)/Mn<sup>4+</sup> and Pt<sup>δ+</sup>/Pt<sup>0</sup> also increased from 2.27 and 2.91 to 3.83 and 4.23, respectively. The content of the Ce<sup>3+</sup> species on the sample surface increased from 9.5 to 10.9%. That is to say, the concentration of Mn<sup>4+</sup> species decreased

while the  $\text{Ce}^{3+}$  species concentration increased. The above results demonstrate that there is an electron transfer ( $\text{Mn}^{4+} + \text{Pt}^0 \rightarrow \text{Mn}^{3+} + \text{Pt}^{\delta+}$ ) [26,27] on the Pt/CeMnO<sub>x</sub>/diatomite sample, which made the Mn species with lower oxidation states be formed. In other words, there was a formation of oxygen vacancies in CeMnO<sub>x</sub>. Hence, the ability of the sample to adsorb and activate oxygen molecules was improved. A higher amount of the O<sub>ads</sub> species on the sample surface favored the oxidation of VOCs [28]. Hence, the Pt/CeMnO<sub>x</sub>/diatomite sample with a higher amount of the O<sub>ads</sub> species showed a much better performance than the Pt/CeMnO<sub>x</sub> sample with a lower amount of the O<sub>ads</sub> species for the oxidation of toluene and ethyl acetate.

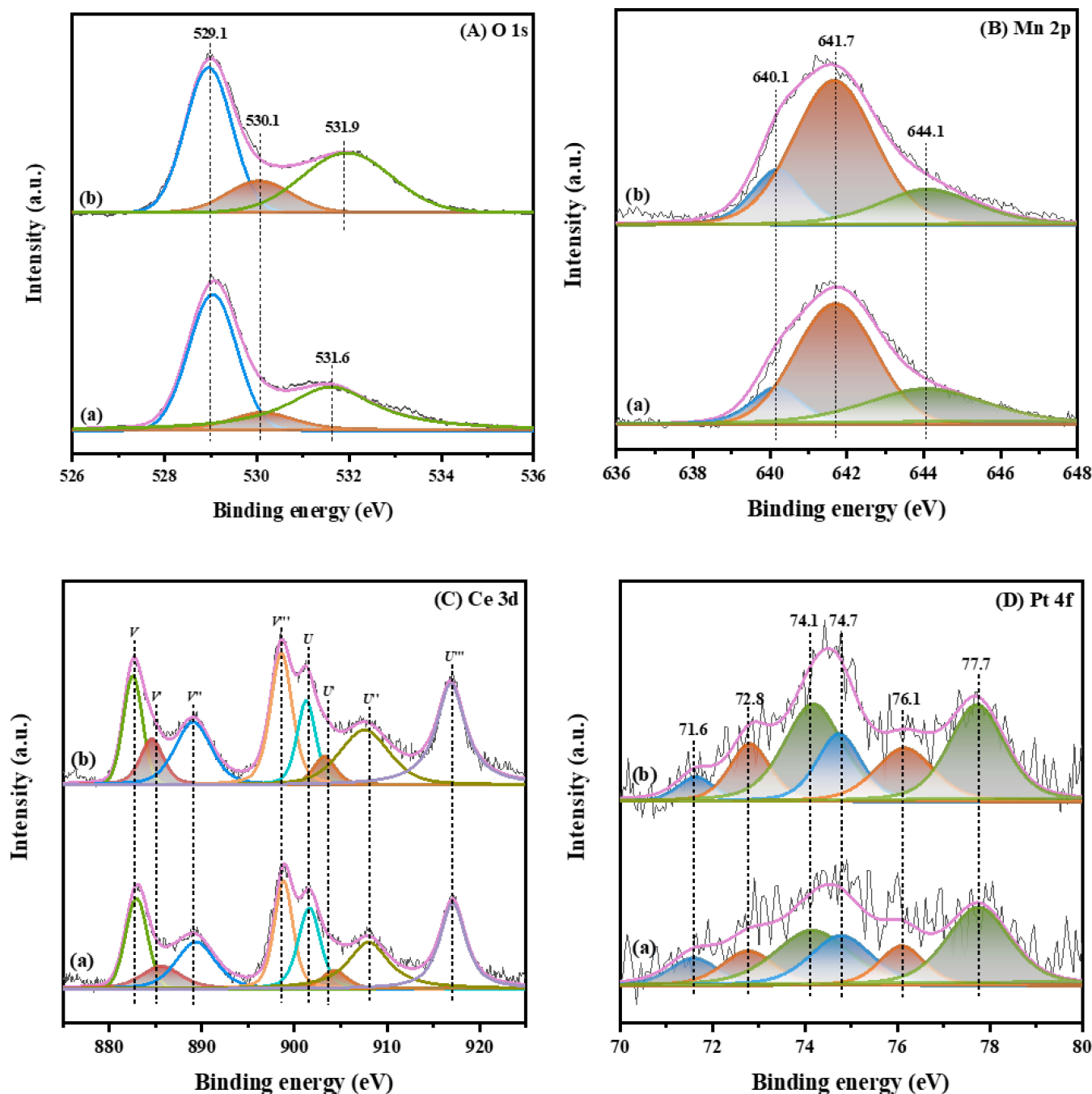


Figure 4. (A) O 1s, (B) Mn 2p, (C) Ce 3d, and (D) Pt 4f XPS spectra of (a) Pt/CeMnO<sub>x</sub> and (b) Pt/CeMnO<sub>x</sub>/diatomite.

#### 2.4. Reducibility

The redox properties of the as-prepared samples were investigated by the H<sub>2</sub>-TPR technique. The H<sub>2</sub>-TPR profiles of the samples and their H<sub>2</sub> consumption are shown in Figure 5 and Table 2, respectively. For the CeMnO<sub>x</sub> (Figure 5a) and CeMnO<sub>x</sub>/diatomite (Figure 5b) samples, the reduction peaks above 600 °C were assigned to the reduction of the bulk Ce species, while those in the range of 200–600 °C were related to the reduction of the surface Mn and Ce species [29,30]. The peaks in the range of 200–600 °C were decomposed into four peaks (denoted as peaks  $\alpha$ ,  $\beta$ ,  $\gamma$ , and  $\delta$ ), as shown in Figure S4. For the CeMnO<sub>x</sub> sample, there were peak  $\alpha$  at 269 °C, peak  $\beta$  at 301 °C, and peak  $\gamma$  at 369 °C, which were related to the reduction processes of MnO<sub>2</sub> → Mn<sub>2</sub>O<sub>3</sub>, Mn<sub>2</sub>O<sub>3</sub> → Mn<sub>3</sub>O<sub>4</sub>, and Mn<sub>3</sub>O<sub>4</sub> → MnO [31,32], respectively. Peak  $\delta$  at 437 °C was assigned to the reduction of Ce<sup>4+</sup> → Ce<sup>3+</sup> [33]. The reduction peak heights of CeMnO<sub>x</sub>/diatomite were slightly higher than those of CeMnO<sub>x</sub>; furthermore, the reduction temperatures of the former were lower than those of the latter. Such a result might be due to the high dispersion of CeMnO<sub>x</sub> on the surface of diatomite, which was favorable for the reduction of CeMnO<sub>x</sub> in the CeMnO<sub>x</sub>/diatomite sample. The reduction peaks of the samples were changed significantly after the loading of Pt. According to the previous literature, the reduction peaks in the low temperature are attributed to the reduction of PtO<sub>x</sub>. Combined with the obtained XPS results, we can realize that the Pt on the sample surface mainly exists in the form of metallic Pt<sup>0</sup> species. Two reduction peaks of the Pt/CeMnO<sub>x</sub>/diatomite sample were observed in the range of 150–500 °C, while only one reduction peak was detected in the Pt/CeMnO<sub>x</sub> sample. The peaks in the range of 285–314 °C corresponded to the reduction of the adsorbed oxygen species, resulting from the interaction between the Pt species and the diatomite support. It is well known that the area of the reduction peak reflects the reducibility of a catalyst to some extent. According to the previous study [33], reducibility was an important factor affecting the catalytic performance of a catalyst. The H<sub>2</sub> consumption can reflect the reducibility of the catalyst, and the reducibility is related to the adsorbed oxygen species on the sample surface. Good reducibility is beneficial for the redox cycle of the catalysts, thus rendering them to show high oxidation activities. We have conducted quantitative analysis on the reduction peaks in the H<sub>2</sub>-TPR profiles of the samples (the quantitative analysis method can be seen in the Supplementary Materials) and the reduction peaks were calibrated against that of the complete reduction of a known standard powered CuO (Aldrich, Saint Louis, American, 99.995%) sample. It can be seen from Table 2 that, although the H<sub>2</sub> consumption of the samples was close, Pt/CeMnO<sub>x</sub>/diatomite exhibits the lowest reduction temperature. Hence, the Pt/CeMnO<sub>x</sub>/diatomite sample with the best low-temperature reducibility showed the best catalytic activity for the oxidation of VOCs.

#### 2.5. Oxygen, Sulfur Dioxide, and VOC Desorption Behaviors

The adsorption behaviors of the oxygen in the samples were measured by the O<sub>2</sub>-TPD technique, and their O<sub>2</sub>-TPD profiles are shown in Figure 6A. The peaks below 300 °C were assigned to the desorption of the surface adsorbed oxygen species, and the ones in the range of 300–600 °C and above 600 °C were attributed to the removal of the surface lattice oxygen species and the bulk lattice oxygen species [34], respectively. It is seen that there is a higher amount of oxygen desorption from the Pt/CeMnO<sub>x</sub>/diatomite sample than from the Pt/CeMnO<sub>x</sub> sample. Such a result was in good consistency with the result obtained by the previous XPS characterization.

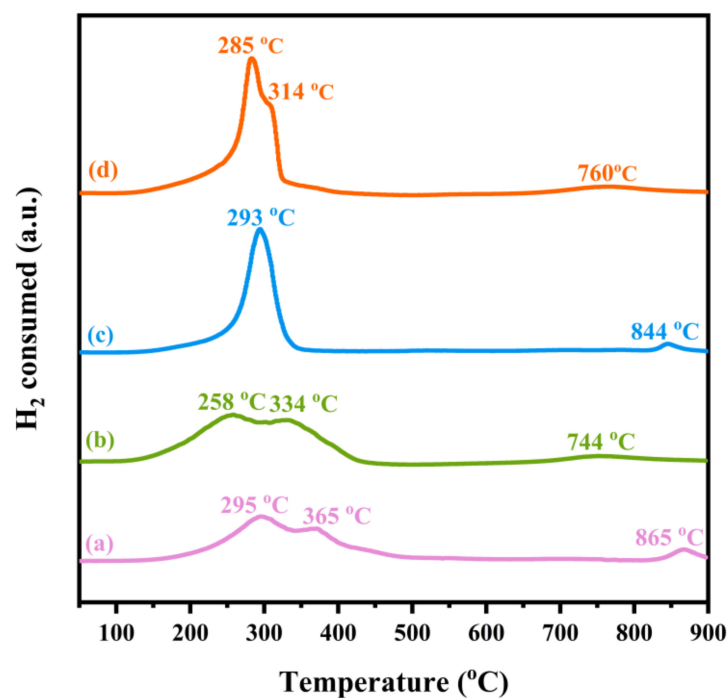


**Figure 5.** H<sub>2</sub>-TPR profiles of (a) CeMnO<sub>x</sub>, (b) CeMnO<sub>x</sub>/diatomite, (c) Pt/CeMnO<sub>x</sub>, and (d) Pt/CeMnO<sub>x</sub>/diatomite.

Figure 6B–D shows the results of the VOC (ethyl acetate + toluene)-TPD of the Pt/CeMnO<sub>x</sub>/diatomite and Pt/CeMnO<sub>x</sub> samples. It is observed that ethyl acetate and toluene are adsorbed on both samples after the oxygen pretreatment. As shown in Figure 6B, the adsorption of ethyl acetate on the Pt/CeMnO<sub>x</sub>/diatomite sample was detected with two desorption peaks at 183 and 381 °C, respectively. In contrast, for the Pt/CeMnO<sub>x</sub> sample, only one desorption peak was recorded at 440 °C. The desorption peak in the low temperature was assigned to the surface adsorption of ethyl acetate, while the ones at 381 and 440 °C were attributed to the chemical adsorption of ethyl acetate. Therefore, the Pt/CeMnO<sub>x</sub>/diatomite sample possessed better ethyl acetate adsorption behavior than the Pt/CeMnO<sub>x</sub> sample; thus, the former outperformed the latter for ethyl acetate oxidation. For the toluene adsorption (Figure 6C), the toluene adsorption capacities of the two samples were similar, and a prominent desorption peak was observed at 423 and 445 °C, respectively. Additionally, CO<sub>2</sub> ( $m/z = 44$ ) production signals were also detected, as shown in Figure 6D. It can be inferred that the formation of CO<sub>2</sub> in the ranges of 200–400 and 400–600 °C is attributed to the reaction of adsorbed toluene and ethyl acetate with the surface adsorbed oxygen and surface lattice oxygen species, respectively. The locations of the CO<sub>2</sub> desorption peaks from the two samples were similar, indicating that the paths of toluene and ethyl acetate oxidation over the two samples were also the same. That is to say, toluene and ethyl acetate were oxidized over the Pt/CeMnO<sub>x</sub>/diatomite and Pt/CeMnO<sub>x</sub> samples according to the same reaction mechanism. The TGA technique was used to analyze weight losses of the diatomite, Pt/CeMnO<sub>x</sub>, and Pt/CeMnO<sub>x</sub>/diatomite samples, and their TGA profiles are shown in Figure S5. From the TGA profiles (Figure S5), one can observe that there are gradual and small weight losses of about 1.0, 3.2, and 1.5 wt% in the RT–300 °C range of the diatomite, Pt/CeMnO<sub>x</sub>, and Pt/CeMnO<sub>x</sub>/diatomite samples, respectively, which are due to the removal of the adsorbed H<sub>2</sub>O and CO<sub>2</sub> as well as the adsorbed oxygen species on the Pt/CeMnO<sub>x</sub> and Pt/CeMnO<sub>x</sub>/diatomite samples. Such a small weight loss means that no structural destruction takes place in the Pt/CeMnO<sub>x</sub>/diatomite. In other words, the Pt/CeMnO<sub>x</sub>/diatomite possessed good structural stability.

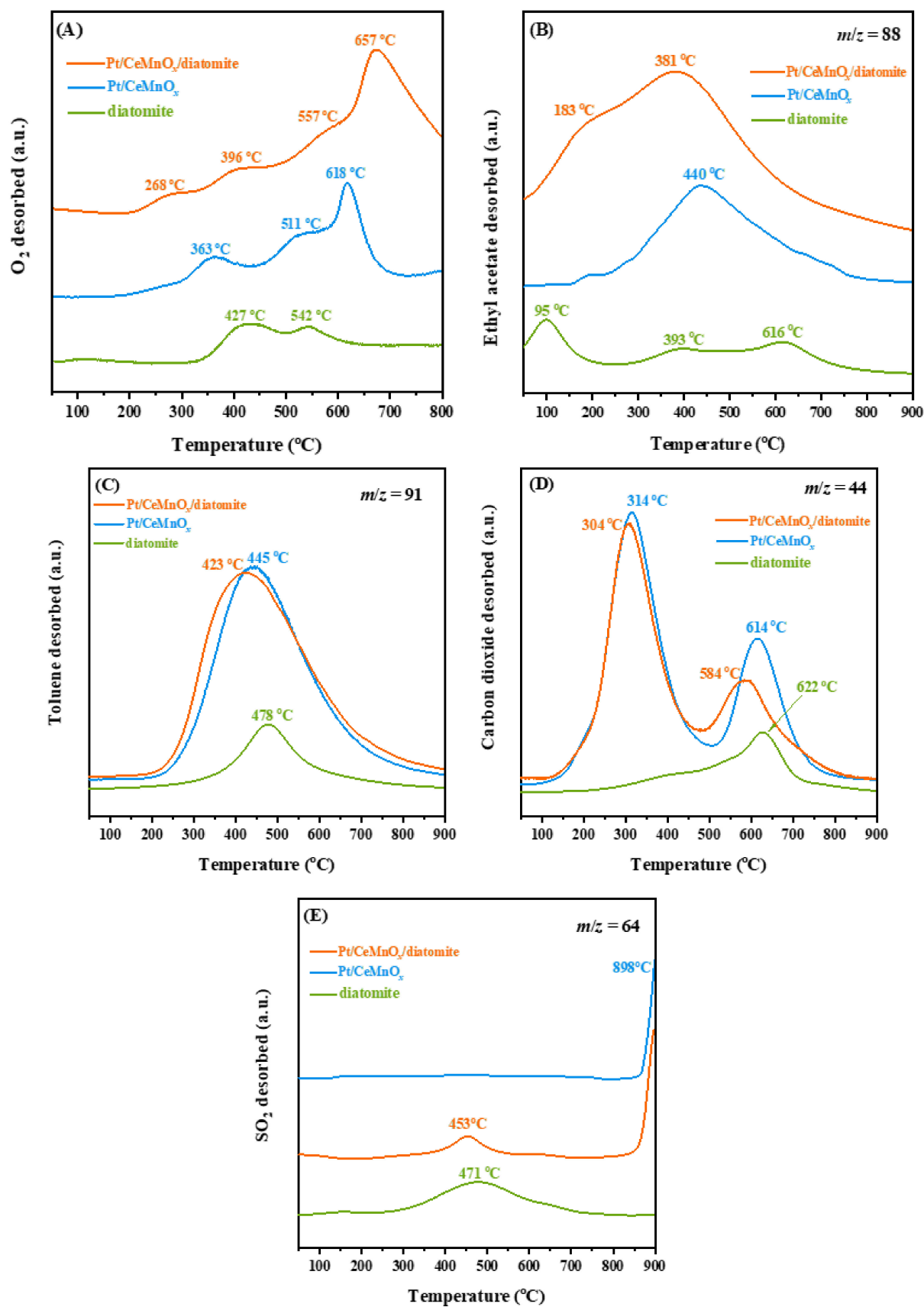
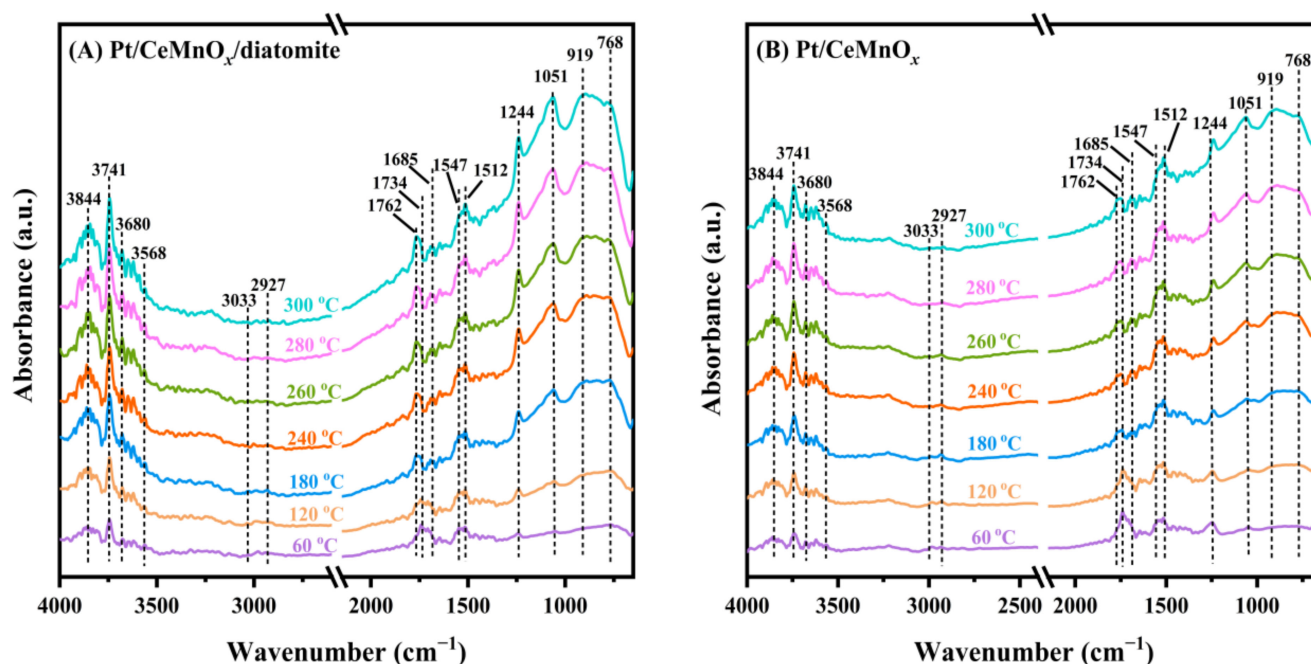


Figure 6. (A) O<sub>2</sub>-TPD, (B–D) (EA + toluene)-TPD, and (E) SO<sub>2</sub>-TPD profiles of the diatomite, Pt/CeMnO<sub>x</sub>/diatomite, and Pt/CeMnO<sub>x</sub> samples.

The SO<sub>2</sub> desorption behaviors of the samples were measured using the SO<sub>2</sub>-TPD technique, and their results are shown in Figure 6E. For the diatomite support, there was one broad desorption peak in the range of 300–700 °C, which was assigned to the desorption of SO<sub>2</sub> adsorbed on the surface of diatomite. One SO<sub>2</sub> desorption peak at a similar temperature was also observed for the Pt/CeMnO<sub>x</sub>/diatomite sample, but no SO<sub>2</sub> desorption peaks were detected for the diatomite-free Pt/CeMnO<sub>x</sub> sample. That is to say, a certain amount of SO<sub>2</sub> was adsorbed on the diatomite support and no SO<sub>2</sub> was adsorbed on the Pt/CeMnO<sub>x</sub> surface. This result reveals that the use of diatomite as a support was beneficial for protecting the active Pt and CeMnO<sub>x</sub> sites from being poisoned by SO<sub>2</sub>, thus enhancing the SO<sub>2</sub> resistance of the Pt/CeMnO<sub>x</sub>/diatomite sample. In addition, the Pt/CeMnO<sub>x</sub> or Pt/CeMnO<sub>x</sub>/diatomite sample displayed a distinct high-temperature desorption peak at approximately 898 °C, which was due to the decomposition of the manganese sulfate species [35]. The stable manganese sulfate species could cover part of the active sites, thus leading to a partial deactivation of the catalysts.

### 2.6. In Situ DRIFTS Spectra of Toluene and Ethyl Acetate Oxidation

In situ DRIFTS characterization was performed to further analyze the detailed intermediates and products of catalytic toluene and ethyl acetate oxidation. The reactant mixture used in the in situ DRIFTS experiments was the same as that used in activity evaluation. After activation in an oxygen atmosphere for 1 h, in situ DRIFTS spectra of Pt/CeMnO<sub>x</sub> and Pt/CeMnO<sub>x</sub>/diatomite at different temperatures were recorded, respectively, and the results are shown in Figure 7. The characteristic band at 3033 cm<sup>-1</sup> was attributed to the C–H bond stretching vibration of aromatic ring in toluene, and the one at 2927 cm<sup>-1</sup> was assigned to the asymmetric stretching vibration of C–H bond in methyl group of toluene [36]. The characteristic band at 1512 cm<sup>-1</sup> corresponded to the out-plane deformation vibration of the benzene ring in toluene [37]. The recording of the OH group interacting with the methyl group at 3680 and 3741 cm<sup>-1</sup> confirms the adsorption of toluene on the surface of the sample [38]. The characteristic band at 1051 cm<sup>-1</sup> was ascribed to the O–O stretching vibration of the chemically adsorbed oxygen species [39]. With the rise in temperature, the area of the band gradually increased. As can be seen from Figure 7, the intensity of the band for the Pt/CeMnO<sub>x</sub>/diatomite sample was stronger than that for the Pt/CeMnO<sub>x</sub> sample. This result shows that the adsorbed oxygen concentration on the former is higher than that on the latter, which is more conducive to the catalytic oxidation of toluene or ethyl acetate. The band at 1734 cm<sup>-1</sup> was attributed to the C–O stretching vibration of ethyl acetate, the one at 1244 cm<sup>-1</sup> was ascribed to the C–O stretching vibration of surface alcoholates, and the one at 1547 cm<sup>-1</sup> was attributed to the COO<sup>-</sup> anti-symmetric stretching vibration of surface acetates [40,41]. The characteristic absorption band at 1685 cm<sup>-1</sup> was due to the C=O stretching vibration of the aldehyde, and the one at 1762 cm<sup>-1</sup> was owing to the C=O stretching vibration of the carboxylic acid. The result demonstrates that ethanol and acetaldehyde are produced in the oxidation of ethyl acetate. The band at 3568 cm<sup>-1</sup> was due to the hydroxyl group on the sample surface [42], and the one at 3844 cm<sup>-1</sup> was assigned to the bridged water [43]. H<sub>2</sub>O (with the bands at 3568, 3680, 3741, and 3844 cm<sup>-1</sup>) increased with the rise in temperature. Hence, the approximate pathways of ethyl acetate or toluene oxidation could be obtained. The C–C and C–O in ethyl acetate are first broken to form the CH<sub>3</sub>CH<sub>2</sub>O\* and CH<sub>3</sub>CO\* species. Then, the intermediates, such as ethanol and acetaldehyde, are produced, and these intermediates are finally converted to CO<sub>2</sub> and H<sub>2</sub>O [44,45]. In the oxidation process of toluene, the intermediate products, such as benzaldehyde and benzoic acid, may be formed, which are finally oxidized to CO<sub>2</sub> and H<sub>2</sub>O. It should be noted that the mechanisms of ethyl acetate or toluene oxidation were similar over the Pt/CeMnO<sub>x</sub>/diatomite and Pt/CeMnO<sub>x</sub> samples.



**Figure 7.** In situ DRIFTS spectra of 1000 ppm toluene and 1000 ppm ethyl acetate oxidation over the Pt/CeMnO<sub>x</sub>/diatomite and Pt/CeMnO<sub>x</sub> samples (after activation treatment in an O<sub>2</sub> flow at 300 °C) at different temperatures.

### 2.7. Catalytic Performance for Toluene and Ethyl Acetate Oxidation

Toluene and ethyl acetate are the typical VOCs in aromatics and esters, respectively, which are widely used in petroleum processing, coating, pharmaceutical, and automobile manufacturing industries. Such components usually exist in the mixture of VOCs emitted in the actual industrial production activities. Hence, taking toluene and ethyl acetate as the model VOCs for their oxidative removal is of significance for industrial applications. Catalytic activities of the samples were evaluated for the oxidation of a VOC mixture (i.e., 1000 ppm ethyl acetate and 1000 ppm toluene), and their results are shown in Figure 8A.

In order to examine the effects of the Ce/Mn molar ratio or noble metal (Pt or Pd) on catalytic performance, we measured the catalytic activities of the samples with Ce/Mn molar ratios of 1:2, 1:1, and 2:1 or the supported Pt or Pd samples under the same reaction conditions, and their results are summarized in Table 3. We used the reaction temperatures ( $T_{50\%}$  and  $T_{90\%}$ ) required for achieving toluene or ethyl acetate conversions of 50 and 90% to evaluate catalytic activities of the samples, respectively. The  $T_{90\%}$  over 0.32Pt/CeMnO<sub>x</sub>/diatomite was lower than that over 0.27Pd/CeMnO<sub>x</sub>/diatomite by 19 °C for ethyl acetate oxidation or 26 °C for toluene oxidation, indicating that the supported Pt sample outperformed the supported Pd sample for the two reactions. Over the samples with different Ce/Mn molar ratios, ethyl acetate conversion first increased and then decreased with the rise in Mn content. For toluene oxidation, the performance of the samples with Ce/Mn molar ratios of 0.5 and 1 was similar but better than the sample with a Ce/Mn molar ratio of 2. Therefore, the Pt/CeMnO<sub>x</sub>/diatomite sample with Ce/Mn molar ratio = 1 was used in the subsequent investigations.

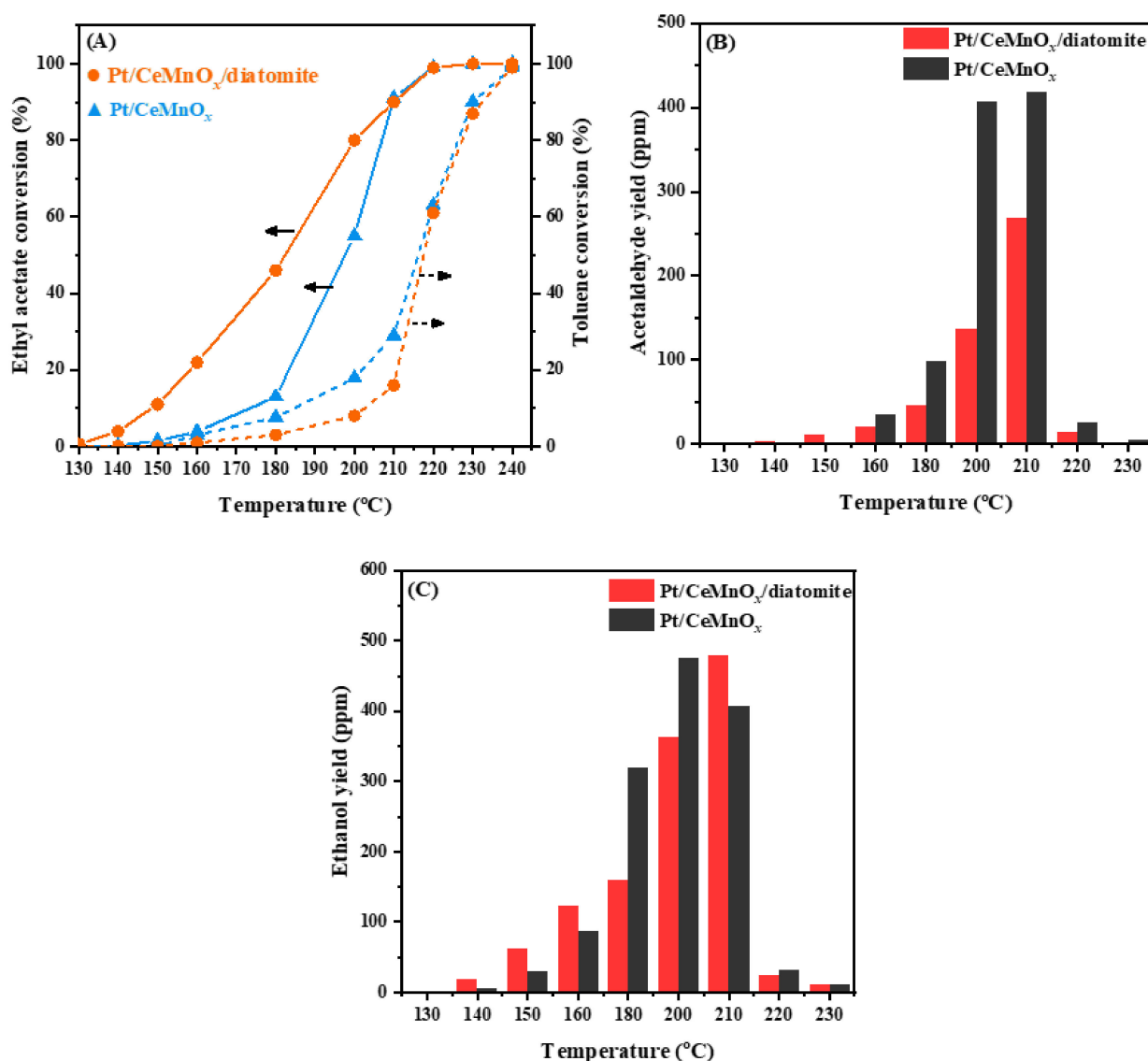


**Figure 8.** (A) Ethyl acetate or toluene conversion, (B) acetaldehyde yield, and (C) ethanol yield as a function of reaction temperature over the Pt/CeMnO<sub>x</sub> and Pt/CeMnO<sub>x</sub>/diatomite samples.

**Table 3.** Catalytic activities of the samples for ethyl acetate and toluene oxidation at SV = 20,000 mL g<sup>-1</sup> h<sup>-1</sup>.

Sample	Toluene Oxidation Activity			Toluene Oxidation at 220 °C		Ethyl Acetate Oxidation Activity			Ethyl Acetate Oxidation at 200 °C	
	T <sub>50%</sub> (°C)	T <sub>90%</sub> (°C)	E <sub>a</sub> (kJ mol <sup>-1</sup> )	TOF <sub>Pt or Pd</sub> (×10 <sup>-3</sup> s <sup>-1</sup> )	Specific Reaction Rate (μmol g <sub>cat</sub> <sup>-1</sup> s <sup>-1</sup> )	T <sub>50%</sub> (°C)	T <sub>90%</sub> (°C)	E <sub>a</sub> (kJ mol <sup>-1</sup> )	TOF <sub>Pt or Pd</sub> (×10 <sup>-3</sup> s <sup>-1</sup> )	Specific Reaction Rate (μmol g <sub>cat</sub> <sup>-1</sup> s <sup>-1</sup> )
0.27Pt/CeMnO <sub>x</sub> /diatomite	236	259	76	22.4	0.61	211	229	55	8.9	0.27
0.32Pt/CeMnO <sub>x</sub> /diatomite	218	233	69	30.2	1.56	182	210	38	22.8	1.04
0.33Pt/CeMn <sub>2</sub> O <sub>x</sub> /diatomite	220	230	67	21.1	1.06	196	212	50	13.5	0.68
0.30Pt/CeMn <sub>0.5</sub> O <sub>x</sub> /diatomite	228	245	72	15.4	0.59	205	221	54	8.3	0.31
0.33Pt/CeMnO <sub>x</sub>	216	230	61	25.7	1.29	200	210	42	7.3	0.42

Figure 8A shows the catalytic activities of the Pt/CeMnO<sub>x</sub>/diatomite and Pt/CeMnO<sub>x</sub> samples for toluene and ethyl acetate oxidation. The reaction sequence of the mixed VOCs over the samples was reflected by the trend in the conversion of ethyl acetate and toluene. Ethyl acetate was first converted and toluene was then oxidized. Over the

Pt/CeMnO<sub>x</sub>/diatomite sample, the catalytic activity of converting ethyl acetate in the VOC mixture at low temperatures was better than that over the Pt/CeMnO<sub>x</sub> sample. The  $T_{50\%}$  values over the Pt/CeMnO<sub>x</sub>/diatomite and Pt/CeMnO<sub>x</sub> samples were 185 and 200 °C, respectively, but the  $T_{90\%}$  values over the two samples were the same (210 °C) for the conversion of ethyl acetate. The above result indicates that the Pt/CeMnO<sub>x</sub>/diatomite sample exhibits better activity than the Pt/CeMnO<sub>x</sub> sample at low temperatures, which is related to the enhanced ethyl acetate adsorption capacity of the former sample. The oxidation of ethyl acetate over the samples obeyed a Mars–van Krevelen mechanism [46]. The Pt nanoparticles and oxygen vacancies on the surface of CeMnO<sub>x</sub> were the key active centers for the VOC oxidation. According to the XPS characterization results, one can realize that the Pt/CeMnO<sub>x</sub>/diatomite sample exhibits the strongest ability to adsorb and activate oxygen molecules, thus making this sample show the best catalytic performance for the VOC oxidation. However, there were no significant differences in toluene conversion over the Pt/CeMnO<sub>x</sub> and Pt/CeMnO<sub>x</sub>/diatomite samples, which displayed the close  $T_{50\%}$  (216 and 218 °C) and  $T_{90\%}$  (233 and 230 °C) values, respectively. Such a result was caused by the similar active sites with rather close Pt loadings (0.32–0.33 wt%). Figure 8B,C show the acetaldehyde and ethanol yields produced during the oxidation of ethyl acetate. The ethanol yields over the Pt/CeMnO<sub>x</sub> and Pt/CeMnO<sub>x</sub>/diatomite samples were close, but there was a significant difference in acetaldehyde yield over the two samples. The amount of acetaldehyde over the Pt/CeMnO<sub>x</sub>/diatomite sample was much lower than that over the Pt/CeMnO<sub>x</sub> sample. The diatomite has a surface with abundant hydroxyl groups and strong adsorption ability [12]. Some of the reactants and intermediates produced in ethyl acetate oxidation could be adsorbed on diatomite. Hence, the use of diatomite as a support would play an important role in improving the activity and selectivity of ethyl acetate oxidation over the diatomite-supported noble metal catalysts.

The turnover frequencies (TOF<sub>S<sub>Pt</sub> or Pd</sub>) and specific reaction rates of the samples for the oxidation of ethyl acetate and toluene were calculated according to their activity data, as summarized in Table 3. Obviously, the 0.32Pt/CeMnO<sub>x</sub>/diatomite sample exhibited the highest TOF<sub>Pt</sub> value and the highest specific reaction rate for the oxidation at 220 °C of ethyl acetate (1.04 μmol g<sub>cat</sub><sup>-1</sup> s<sup>-1</sup>) or toluene (1.56 μmol g<sub>cat</sub><sup>-1</sup> s<sup>-1</sup>). Table S1 summarizes the VOC oxidation activities of the catalysts presented in this work and reported in the literature. It can be found that the 0.32Pt/CeMnO<sub>x</sub>/diatomite catalyst prepared in the present work performed better than the previously reported catalysts in the oxidation of VOC mixtures.

In the past few years, there have been a lot of research works related to the kinetics of catalytic VOC oxidation. For example, Behar et al. [47] claimed that toluene combustion over Cu<sub>1.5</sub>Mn<sub>1.5</sub>O<sub>4</sub> was first- and zero-order with respect to toluene and oxygen concentrations, respectively. Chen et al. [48] found that CH<sub>2</sub>Cl<sub>2</sub> oxidation over Au/Co<sub>3</sub>O<sub>4</sub> was first- and zero-order toward CH<sub>2</sub>Cl<sub>2</sub> and O<sub>2</sub> concentrations, respectively. In one of our previous works, a similar reaction mechanism over the Pd/meso-CoO and Pd/meso-Co<sub>3</sub>O<sub>4</sub> catalysts was also confirmed [49]. Hence, it can be reasonably assumed that the oxidation of toluene and ethyl acetate in an excessive-oxygen (VOC/O<sub>2</sub> molar ratio = 1/400) atmosphere obeys a first-order reaction mechanism with respect to VOC concentration ( $c$ ):  $r = -kc = (-A\exp(-E_a/RT))c$ , where  $r$ ,  $k$ ,  $A$ , and  $E_a$  are the reaction rate (mol s<sup>-1</sup>), rate constant (s<sup>-1</sup>), pre-exponential factor, and apparent activation energy (kJ mol<sup>-1</sup>), respectively. The Arrhenius plots for the oxidation of toluene and ethyl acetate over the samples and the  $E_a$  values with standard deviations are shown in Figure S3. It should be noted that the standard deviations of the  $E_a$  values were 1.1–3.9 kJ mol<sup>-1</sup> for toluene oxidation, while they were 2.9–5.2 kJ mol<sup>-1</sup> for ethyl acetate oxidation over the Pt/CeMnO<sub>x</sub>, Pt/CeMn<sub>2</sub>O<sub>x</sub>/diatomite, Pt/CeMnO<sub>x</sub>/diatomite, Pt/CeMn<sub>0.5</sub>O<sub>x</sub>/diatomite, and Pd/CeMnO<sub>x</sub>/diatomite samples. The  $E_a$  value of toluene oxidation decreased in the order of 0.27Pd/CeMnO<sub>x</sub>/diatomite (76 kJ mol<sup>-1</sup>) > 0.30Pt/CeMn<sub>0.5</sub>O<sub>x</sub>/diatomite (72 kJ mol<sup>-1</sup>) > 0.32Pt/CeMnO<sub>x</sub>/diatomite (69 kJ mol<sup>-1</sup>) > 0.33Pt/CeMn<sub>2</sub>O<sub>x</sub>/diatomite (67 kJ mol<sup>-1</sup>) > 0.33Pt/CeMnO<sub>x</sub> (61 kJ mol<sup>-1</sup>). For ethyl acetate oxidation, it decreased in

the sequence of 0.27Pd/CeMnO<sub>x</sub>/diatomite (55 kJ mol<sup>-1</sup>) > 0.30Pt/CeMn<sub>0.5</sub>O<sub>x</sub>/diatomite (54 kJ mol<sup>-1</sup>) > 0.33Pt/CeMn<sub>2</sub>O<sub>x</sub>/diatomite (50 kJ mol<sup>-1</sup>) > 0.33Pt/CeMnO<sub>x</sub> (42 kJ mol<sup>-1</sup>) > 0.32Pt/CeMnO<sub>x</sub>/diatomite (38 kJ mol<sup>-1</sup>), which was in good consistency with their activity changing trend.

### 2.8. Surface Element Compositions of the Samples after SO<sub>2</sub> Treatment

The adsorbed oxygen species, surface element compositions, and metal oxidation state distributions of the samples before and after SO<sub>2</sub> treatment were determined by the XPS technique, and their results are shown in Figure 9A–E and Table 4. After SO<sub>2</sub> treatment, the O<sub>ads</sub>/O<sub>latt</sub> molar ratio decreased, but the Mn<sup>2+</sup>/Mn<sup>δ+</sup> (Mn<sup>δ+</sup> = Mn<sup>2+</sup> + Mn<sup>3+</sup> + Mn<sup>4+</sup>) molar ratios on the Pt/CeMnO<sub>x</sub> and Pt/CeMnO<sub>x</sub>/diatomite samples increased. For the Pt/CeMnO<sub>x</sub> sample, the Mn<sup>2+</sup>/Mn<sup>δ+</sup> molar ratio increased from 0.12 to 0.39, much higher than that (from 0.18 to 0.34) on the Pt/CeMnO<sub>x</sub>/diatomite sample. In addition, the Pt<sup>2+</sup>/Pt<sup>δ+</sup> (Pt<sup>δ+</sup> = Pt<sup>0</sup> + Pt<sup>2+</sup> + Pt<sup>4+</sup>) and S<sup>6+</sup>/S<sup>4+</sup> molar ratios on the Pt/CeMnO<sub>x</sub> sample were also higher than those on the Pt/CeMnO<sub>x</sub>/diatomite sample. The results reveal that SO<sub>2</sub> molecules attached to the Pt and Mn active sites tended to form a higher amount of sulfate on the surface of Pt/CeMnO<sub>x</sub>, as compared with the Pt/CeMnO<sub>x</sub>/diatomite sample surface. This also indicates that a certain amount of SO<sub>2</sub> can be adsorbed by the diatomite. Hence, the use of diatomite as a support could protect the active sites in the sample to a certain extent.

**Table 4.** Surface element compositions of the fresh and SO<sub>2</sub>-treated samples.

Sample	Surface Element Molar Ratio (mol/mol)				
	Pt <sup>2+</sup> /Pt <sup>δ+</sup>	Mn <sup>2+</sup> /Mn <sup>δ+</sup>	Ce <sup>3+</sup> /(Ce <sup>4+</sup> + Ce <sup>3+</sup> )	O <sub>ads</sub> /O <sub>latt</sub>	S <sup>6+</sup> /S <sup>4+</sup>
Pt/CeMnO <sub>x</sub>	0.20	0.12	0.09	0.21	–
Pt/CeMnO <sub>x</sub> /diatomite	0.26	0.18	0.10	0.29	–
Pt/CeMnO <sub>x</sub> (SO <sub>2</sub> -treated)	0.30	0.39	0.12	0.16	3.21
Pt/CeMnO <sub>x</sub> /diatomite (SO <sub>2</sub> -treated)	0.22	0.34	0.10	0.25	2.44

### 2.9. Sulfur Dioxide and Water Resistance

Sulfur oxide is a common component in industrial waste gas. Usually, SO<sub>2</sub> can be strongly adsorbed on the surface of a catalyst by forming the sulfate species, occupying the active sites and hence resulting in catalyst deactivation. Such a deactivation is usually irreversible. Therefore, the existence of SO<sub>2</sub> will significantly affect the lifetime of a catalyst. There was a competitive adsorption between reactants and sulfur dioxide during the VOC oxidation process in the presence of SO<sub>2</sub>. In the meanwhile, SO<sub>2</sub> could also lead to the deactivation of the catalysts, thus influencing the oxidation of toluene or ethyl acetate. However, the catalysts with good SO<sub>2</sub> resistance could still show high catalytic activities and stability in toluene and ethyl acetate oxidation in the presence of SO<sub>2</sub>.

In order to explore the SO<sub>2</sub> resistance of the typical samples, we measured the catalytic performance of Pt/CeMnO<sub>x</sub> and Pt/CeMnO<sub>x</sub>/diatomite for the oxidation of ethyl acetate and toluene in the presence of 25 ppm SO<sub>2</sub>. As shown in Figure 10A,B, 25 ppm SO<sub>2</sub> was introduced to the mixed VOC feedstock at T<sub>90%</sub> (210 °C and 230 °C of ethyl acetate and toluene oxidation at SV = 20,000 mL g<sup>-1</sup> h<sup>-1</sup>, respectively). Before the introduction of SO<sub>2</sub>, the conversions of VOCs over Pt/CeMnO<sub>x</sub> or Pt/CeMnO<sub>x</sub>/diatomite were stable at about 90%. When 25 ppm SO<sub>2</sub> was added, ethyl acetate conversion over Pt/CeMnO<sub>x</sub> or Pt/CeMnO<sub>x</sub>/diatomite continued to decrease. After 8 h of on-stream reaction, ethyl acetate conversion was stabilized at 25 and 41%, respectively. After cutting off the SO<sub>2</sub>, ethyl acetate conversion over Pt/CeMnO<sub>x</sub> rose slightly to 37%, while that over Pt/CeMnO<sub>x</sub>/diatomite remained at about 41%.

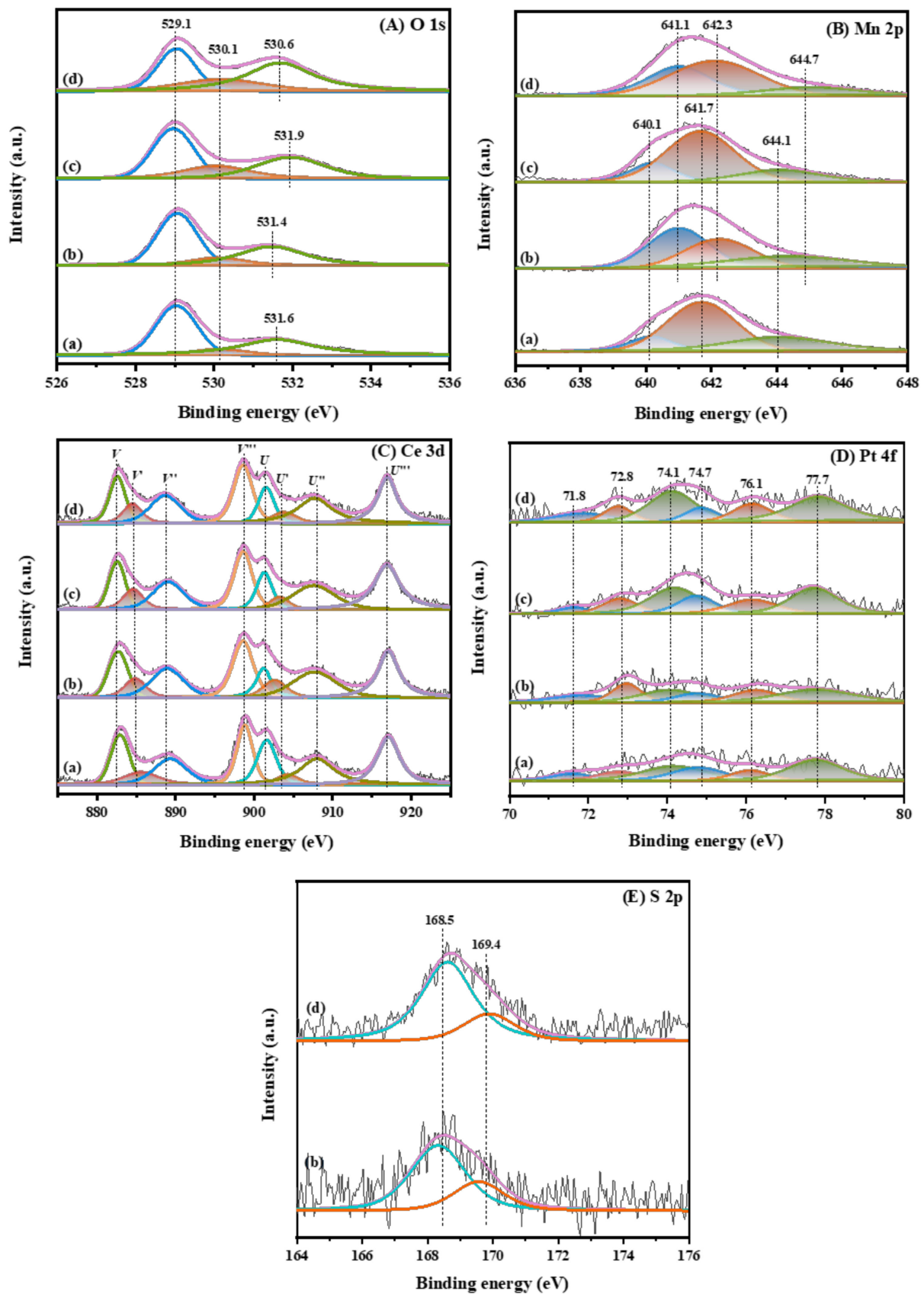


**Figure 9.** (A) O 1s, (B) Mn 2p, (C) Ce 3d, (D) Pt 4f, and (E) S 2p XPS spectra of (a) fresh Pt/CeMnO<sub>x</sub>, (b) Pt/CeMnO<sub>x</sub> after SO<sub>2</sub> treatment, (c) fresh Pt/CeMnO<sub>x</sub>/diatomite, and (d) Pt/CeMnO<sub>x</sub>/diatomite after SO<sub>2</sub> treatment.

The SO<sub>2</sub> resistance during the oxidation of toluene over the samples was tested at 230 °C with other conditions being the same as in activity evaluation, and the results are shown in Figure 9B. Ethyl acetate has already completely converted at this temperature, so SO<sub>2</sub> exerted little effect on ethyl acetate conversion. However, the Pt/CeMnO<sub>x</sub> and Pt/CeMnO<sub>x</sub>/diatomite samples showed different sulfur dioxide resistance in toluene oxidation. Over the Pt/CeMnO<sub>x</sub> sample, catalytic activity decreased rapidly from 91 to 13% in 4 h after the introduction of SO<sub>2</sub>. When SO<sub>2</sub> was cut off, toluene conversion was recovered to 29%, much lower than its initial conversion level. Over the Pt/CeMnO<sub>x</sub>/diatomite sample, however, toluene conversion decreased from 90 to 77% but was still stabilized at this level (about 77%) and not recovered when the SO<sub>2</sub> was cut off. Combined with the XPS results, we can realize that SO<sub>2</sub> is adsorbed on the surface of both samples by forming a large amount of sulfate species. Over the Pt/CeMnO<sub>x</sub> sample, the decrease in the conversion of ethyl acetate or toluene was owing to the generation of the stable sulfate species at different active sites. Over the Pt/CeMnO<sub>x</sub>/diatomite sample, except for forming manganese sulfate on the surface, some SO<sub>2</sub> molecules were adsorbed on diatomite because of its good adsorption property. Therefore, the use of diatomite as a support could protect the active sites from being poisoned to a certain extent. In addition, the active component also existed on the inner surface of the pores due to the unique disc-shaped porous structure of diatomite. Such an active component could still play a catalytic role after adding SO<sub>2</sub>. Because of the pore size, the active component on the inner surface was mostly Pt. Pt is the preferential active site for toluene oxidation over the sample. Hence, this part of Pt in Pt/CeMnO<sub>x</sub>/diatomite might have governed the oxidation of toluene after the sample was treated with SO<sub>2</sub>.

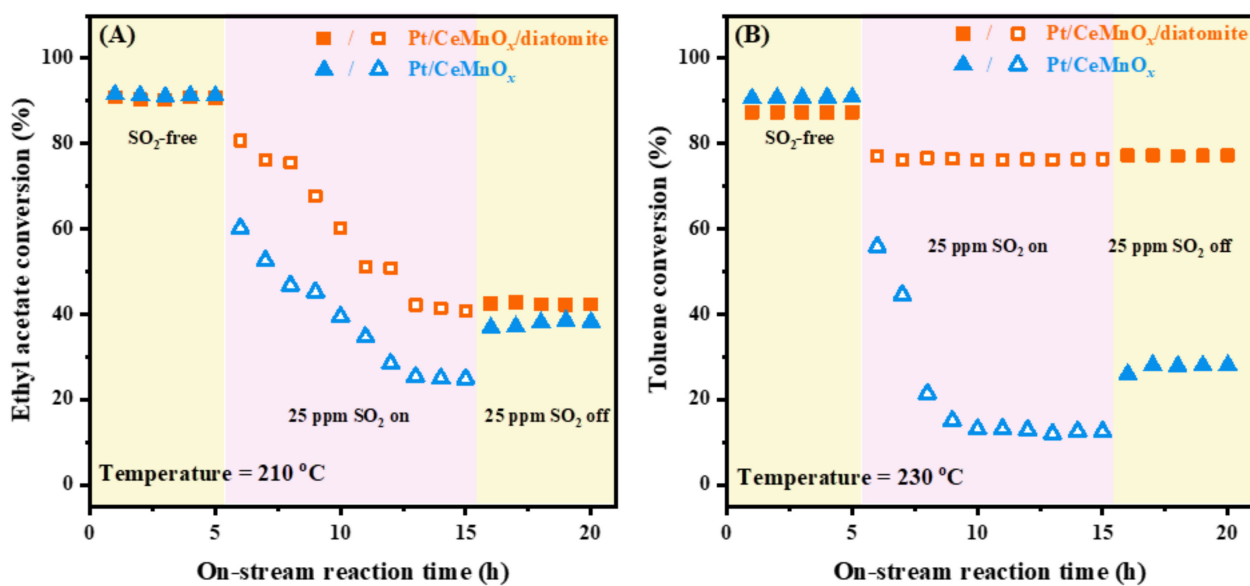


**Figure 10.** Effect of 25 ppm SO<sub>2</sub> on catalytic activity of Pt/CeMnO<sub>x</sub>/diatomite and Pt/CeMnO<sub>x</sub> for (A) ethyl acetate oxidation at 210 °C or (B) toluene oxidation at 230 °C.

Except for the SO<sub>2</sub> effect, the influence of water vapor on catalytic performance cannot also be ignored. In order to examine the effect of H<sub>2</sub>O on the activity of the Pt/CeMnO<sub>x</sub>/diatomite and Pt/CeMnO<sub>x</sub> samples, we carried out toluene and ethyl acetate oxidation in the presence of 5.0 vol% H<sub>2</sub>O, and the results are shown in Figure 11A,B, respectively. Obviously, toluene or ethyl acetate conversions over the two samples decreased with the addition of water vapor. When water vapor was cut off, toluene or ethyl acetate conversions were gradually restored to the initial levels in the absence of water vapor. This phenomenon was attributable to the competitive adsorption between water vapor and the reactants' molecules [50].

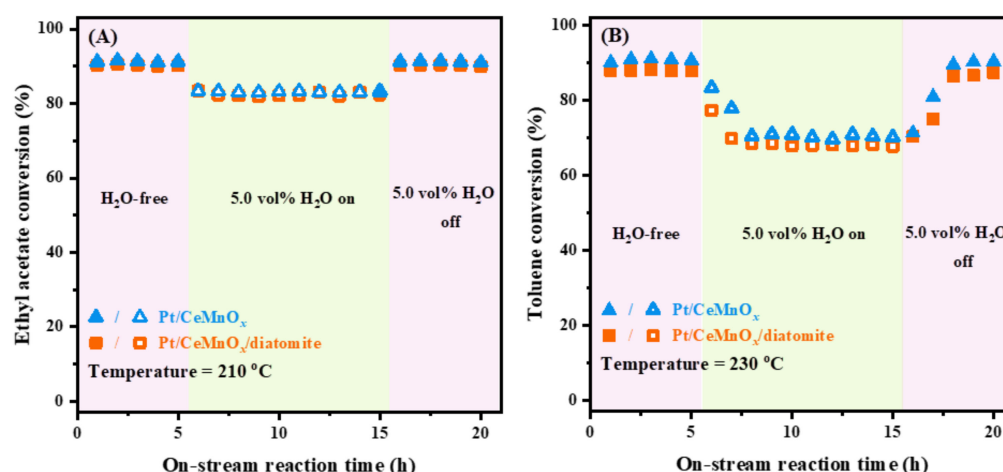


**Figure 11.** Effect of 5.0 vol% H<sub>2</sub>O on catalytic activity of Pt/CeMnO<sub>x</sub>/diatomite and Pt/CeMnO<sub>x</sub> for (A) ethyl acetate oxidation at 210 °C or (B) toluene oxidation at 230 °C.

### 3. Materials and Methods

#### 3.1. Chemical Reagents

Diatomite and H<sub>2</sub>PtCl<sub>6</sub>·6H<sub>2</sub>O were purchased from Macklin (Shanghai, China). Potassium permanganate (KMnO<sub>4</sub>), cerium chloride hexahydrate (CeCl<sub>3</sub>·7H<sub>2</sub>O), manganese chloride tetrahydrate (MnCl<sub>2</sub>·4H<sub>2</sub>O), and sodium hydroxide (NaOH) were purchased from Shanghai Aladdin Biochemical Technology Co., Ltd. All of the reagents were analytical-grade and used without further purification.

#### 3.2. Preparation of CeMnO<sub>x</sub>/Diatomite

The CeMnO<sub>x</sub>/diatomite catalyst was prepared by the redox precipitation method [51]. Amounts of 1.00 g of diatomite, 0.63 g of KMnO<sub>4</sub>, 3.70 g of CeCl<sub>3</sub>·7H<sub>2</sub>O, and 1.20 g of MnCl<sub>2</sub>·4H<sub>2</sub>O were dissolved in 50 mL of deionized water and stirred for 1 h to be dispersed uniformly. Then, 0.2 mol L<sup>-1</sup> of NaOH aqueous solution was added dropwise into the above mixed solution to adjust the pH value to 11.0 under stirring for 4 h. After the solution was centrifugated, the as-obtained solid was repeatedly washed with deionized water until the chloride was completely removed. Finally, the catalyst was dried at 80 °C for 12 h and further calcined in air at 500 °C for 4 h, thus obtaining the CeMnO<sub>x</sub>/diatomite catalyst. In order to compare the effect of Ce/Mn proportion in the CeMnO<sub>x</sub> composites on the catalytic activity of the catalysts, we selected Ce/Mn theoretical stoichiometric ratios of 0.5, 1, and 2, respectively. For comparison purposes, the CeMnO<sub>x</sub>, CeMn<sub>2</sub>O<sub>x</sub>/diatomite, and CeMn<sub>0.5</sub>O<sub>x</sub>/diatomite were also prepared by the same method.

#### 3.3. Preparation of Pt/CeMnO<sub>x</sub>/Diatomite, Pt/CeMnO<sub>x</sub>, Pt/CeMn<sub>2</sub>O<sub>x</sub>/Diatomite, Pt/CeMn<sub>0.5</sub>O<sub>x</sub>/Diatomite, and Pd/CeMnO<sub>x</sub>/Diatomite

The Pt/CeMnO<sub>x</sub>/diatomite catalyst was prepared using a simple incipient wetness impregnation approach. An amount of 500 mg of the CeMnO<sub>x</sub>/diatomite support was impregnated with a certain amount of 0.01 mol L<sup>-1</sup> H<sub>2</sub>PtCl<sub>6</sub>·6H<sub>2</sub>O aqueous solution (theoretical Pt loading = 0.5 wt%) at room temperature for 7 h. The as-obtained wet solid was first dried at 80 °C for 12 h and then calcined in air at 500 °C for 4 h, thus obtaining the Pt/CeMnO<sub>x</sub>/diatomite catalyst. For comparison purposes, the Pt/CeMnO<sub>x</sub>, Pt/CeMn<sub>2</sub>O<sub>x</sub>/diatomite, Pt/CeMn<sub>0.5</sub>O<sub>x</sub>/diatomite, and Pd/CeMnO<sub>x</sub>/diatomite catalysts were also prepared using the above same method. The concentration of the PdCl<sub>2</sub> precursor solution was 0.01 mol L<sup>-1</sup>. The actual Pt and Pd loadings in Pt/CeMnO<sub>x</sub>/diatomite, Pt/CeMnO<sub>x</sub>, Pt/CeMn<sub>2</sub>O<sub>x</sub>/diatomite, Pt/CeMn<sub>0.5</sub>O<sub>x</sub>/diatomite, and Pd/CeMnO<sub>x</sub>/diatomite were 0.32, 0.33, 0.33, 0.30, and 0.27 wt%, respectively, as revealed by the inductively coupled plasma-atomic emission spectroscopic (ICP-AES) characterization results.

### 3.4. Catalyst Characterization

The physicochemical properties of the catalysts were characterized by ICP–AES (Thermo Electron IRIS Intrepid ER/S spectrometer, Waltham, MA, USA), powdered X-ray diffraction XRD, Bruker/AXS D8 Advance diffractometer, with Cu K $\alpha$  radiation and nickel filter ( $\lambda = 0.15406$  nm), Berlin, Germany), scanning electron microscopy (SEM, Gemini Zeiss Supra 55 apparatus, Oberkochen, Germany), N<sub>2</sub> adsorption–desorption (BET, Micromeritics ASAP 2020 analyzer, Norcross, GA, USA), X-ray photoelectron spectroscopy (XPS, Thermo Fisher Scientific ESCALAB 250 Xi spectrometer, Waltham, MA, USA), H<sub>2</sub> temperature-programmed reduction (H<sub>2</sub>-TPR, AutoChem II 2920, Micromeritics, Norcross, GA, USA), O<sub>2</sub> temperature-programmed desorption (O<sub>2</sub>-TPD), and SO<sub>2</sub> temperature-programmed desorption (SO<sub>2</sub>-TPD)(Autochem II 2920, Micromeritics, Norcross, GA, USA, respectively), thermogravimetric analysis (TGA, Setaram Labsys evo, Caluire, France), ethyl acetate or toluene temperature-programmed desorption (EA-TPD or toluene-TPD)(Autochem II 2920, Micromeritics, Norcross, GA, USA), and in situ diffuse reflectance infrared Fourier transform spectroscopy (in situ DRIFTS, Nicolet 6700 FT-IR spectrometer with a liquid-nitrogen-cooled MCT detector, Bruker, Berlin, Germany). The detailed characterization procedures can be seen in the Supplementary Materials.

### 3.5. Catalytic Performance Evaluation

Toluene and ethyl acetate oxidation performance was determined in a fixed-bed quartz tubular microreactor (i.d. = 6 mm). Amounts of 50 mg of the catalyst (40–60 mesh) and 0.25 g of quartz sand (40–60 mesh) were well mixed to minimize the effect of hot spots. Before the test, each sample was pretreated in O<sub>2</sub> (20 mL min<sup>−1</sup>) at 250 °C for 1 h. The measurement conditions were as follows: the gas mixture was 1000 ppm toluene +1000 ppm ethyl acetate +40 vol% O<sub>2</sub> + N<sub>2</sub> (balance), the total flow rate was 16.7 mL min<sup>−1</sup>, and the space velocity (SV) was 20,000 mL g<sup>−1</sup> h<sup>−1</sup>. When the SO<sub>2</sub> or H<sub>2</sub>O was added, 25 ppm SO<sub>2</sub> and 5.0 vol% H<sub>2</sub>O were introduced to the reaction system by a mass controller. The 25 ppm SO<sub>2</sub> came from a gas cylinder, and the 5.0 vol% H<sub>2</sub>O was provided by a water saturator at 34 °C. Reactants and products were analyzed online by gas chromatography (GC-2014C, Shimadzu, Kyoto, Japan), equipped with a flame ionization detector (FID) and a thermal conductivity detector (TCD), using a stabilwax@-DA column (30 m in length) for VOC separation and a 1/8 in Carboxen 1000 column (3 m in length) for permanent gas separation. Two parameters ( $T_{50\%}$  and  $T_{90\%}$ ) were used to measure activities of the samples, which refer to the temperatures achieving 50 and 90% conversions of toluene or ethyl acetate, respectively. Toluene or ethyl acetate conversion was calculated according to the formula:  $(c_{\text{inlet}} - c_{\text{outlet}})/c_{\text{inlet}} \times 100\%$ , where  $c_{\text{inlet}}$  and  $c_{\text{outlet}}$  are the inlet and outlet toluene or ethyl acetate concentrations, respectively.

## 4. Conclusions

The Pt/CeMnO<sub>x</sub> and Pt/CeMnO<sub>x</sub>/diatomite samples were prepared using the redox precipitation and incipient wetness impregnation methods. Among the as-prepared samples, Pt/CeMnO<sub>x</sub>/diatomite exhibited the best catalytic activity ( $T_{90\%} = 210$  °C and 230 °C for ethyl acetate and toluene oxidation at SV = 20,000 mL g<sup>−1</sup> h<sup>−1</sup>, respectively, and TOF<sub>Pt</sub> at 220 °C = 1.04  $\mu\text{mol g}_{\text{cat}}^{-1} \text{s}^{-1}$  for ethyl acetate oxidation and 1.56  $\mu\text{mol g}_{\text{cat}}^{-1} \text{s}^{-1}$  toluene oxidation), as well as an excellent performance especially for ethyl acetate oxidation at low temperatures, with its  $T_{50\%}$  being 20 °C lower than that over the Pt/CeMnO<sub>x</sub> sample at SV = 20,000 mL g<sup>−1</sup> h<sup>−1</sup>. Catalytic activity at low temperatures was improved since diatomite increased the ethyl acetate adsorption capacity of the sample. The Pt/CeMnO<sub>x</sub>/diatomite sample showed a better sulfur dioxide resistance than the Pt/CeMnO<sub>x</sub> sample during the toluene oxidation process due to the fact that the former possesses the unique disc-shaped porous structure and good adsorption property of diatomite. Some of the SO<sub>2</sub> molecules were adsorbed on diatomite due to its excellent adsorption behavior, thus protecting the active sites on the sample surface from being poisoned by SO<sub>2</sub>. The mechanisms of ethyl acetate and toluene oxidation over the Pt/CeMnO<sub>x</sub>/diatomite and Pt/CeMnO<sub>x</sub>

samples were as follows: (i) The C–C and C–O bonds in ethyl acetate are first broken to form the  $\text{CH}_3\text{CH}_2\text{O}^*$  and  $\text{CH}_3\text{CO}^*$  species, and these intermediates are then converted to  $\text{CO}_2$  and  $\text{H}_2\text{O}$ ; (ii) toluene is first oxidized to benzaldehyde and benzoic acid, which are then converted to  $\text{CO}_2$  and  $\text{H}_2\text{O}$ . This work combined the advantages of an active  $\text{CeMnO}_x$  composite and natural diatomite. In addition, the preparation method adopted in this study was simple. The as-prepared  $\text{Pt/CeMnO}_x/\text{diatomite}$  catalyst exhibited good activity for the oxidation of toluene and ethyl acetate. In particular, this catalyst showed good  $\text{SO}_2$  resistance in toluene oxidation. Therefore, the present study is of practical significance. We are sure that such a catalytic material is promising in the practical industrial applications of VOC removal.

**Supplementary Materials:** The following catalyst preparation procedures and catalytic evaluation procedures are available online at <https://www.mdpi.com/article/10.3390/catal13040676/s1>: Table S1, Comparison of catalytic activities for ethyl acetate and toluene oxidation of the  $\text{Pt/CeMnO}_x/\text{diatomite}$  sample prepared in the present work and various catalysts reported in the literature; Figure S1, Ethyl acetate or toluene conversion as a function of reaction temperature over the  $\text{Pd/CeMnO}_x/\text{diatomite}$  and  $\text{Pt/CeMnO}_x/\text{diatomite}$  samples at  $\text{SV} = 20,000 \text{ mL g}^{-1} \text{ h}^{-1}$ ; Figure S2, Ethyl acetate or toluene conversion as a function of reaction temperature over the  $\text{Pt/CeMnO}_x/\text{diatomite}$  samples with different Ce/Mn ratios at  $\text{SV} = 20,000 \text{ mL g}^{-1} \text{ h}^{-1}$ ; Figure S3,  $\ln k$  versus inverse temperature over (a)  $\text{Pt/CeMnO}_x$ , (b)  $\text{Pt/CeMn}_2\text{O}_x/\text{diatomite}$ , (c)  $\text{Pt/CeMnO}_x/\text{diatomite}$ , (d)  $\text{Pt/CeMn}_{0.5}\text{O}_x/\text{diatomite}$ , and (e)  $\text{Pd/CeMnO}_x/\text{diatomite}$  for the oxidation of (A) toluene and (B) ethyl acetate at  $\text{SV} = 20,000 \text{ mL g}^{-1} \text{ h}^{-1}$ ; Figure S4, Deconvoluted reduction peaks in  $\text{H}_2$ -TPR profiles of the  $\text{CeMnO}_x$  and  $\text{CeMnO}_x/\text{diatomite}$  samples; Figure S5, TGA curves of the  $\text{Pt/CeMnO}_x/\text{diatomite}$ ,  $\text{Pt/CeMnO}_x$ , and diatomite samples and references [13,52–59].

**Author Contributions:** Conceptualization, H.D.; Methodology, Y.L. and H.D.; Software, J.D. and L.J.; Investigation, L.L.; Resources, H.D.; Data Curation, L.L., Y.L., J.D. and L.J.; Writing—Original Draft Preparation, L.L.; Writing—Review and Editing, J.D., L.J. and H.D.; Visualization, Z.H. and R.G.; Supervision, Y.L. and H.D.; Project Administration, H.D.; Funding Acquisition, H.D. All authors have read and agreed to the published version of the manuscript.

**Funding:** This work was supported by the National Natural Science Foundation Committee of China–Liaoning Provincial People’s Government Joint Fund (U1908204), National Natural Science Foundation of China (21876006 and 21976009), Natural Science Foundation of Beijing Municipal Commission of Education (KM201710005004), Development Program for the Youth Outstanding–Notch Talent of Beijing Municipal Commission of Education (CIT&TCD201904019), and Foundation on the Creative Research Team Construction Promotion Project of Beijing Municipal Institutions (IDHT20190503).

**Data Availability Statement:** All the relevant data used in this study have been provided in the form of figures and tables in the published article, and all data provided in the present manuscript are available to whomever they may concern.

**Conflicts of Interest:** The authors declare no conflict of interest.

## References

1. He, C.; Cheng, J.; Zhang, X.; Douthwaite, M.; Pattison, S.; Hao, Z.P. Recent advances in the catalytic oxidation of volatile organic compounds: A review based on pollutant sorts and sources. *Chem. Rev.* **2019**, *119*, 4471–4568. [[CrossRef](#)] [[PubMed](#)]
2. Xi, Y.; Reed, C.; Lee, Y.K.; Oyama, S.T. Acetone oxidation using ozone on manganese oxide catalysts. *J. Phys. Chem. B* **2005**, *109*, 17587–17596. [[CrossRef](#)] [[PubMed](#)]
3. Zhang, H.Y.; Sui, S.H.; Zheng, X.M.; Cao, R.R.; Zhang, P.Y. One-pot synthesis of atomically dispersed Pt on  $\text{MnO}_2$  for efficient catalytic decomposition of toluene at low-temperatures. *Appl. Catal. B* **2019**, *257*, 117878. [[CrossRef](#)]
4. Darif, B.; Ojala, S.; Pirault-Roy, L.; Bensitel, M.; Brahmi, R.; Keiski, R.L. Study on the catalytic oxidation of DMDS over Pt-Cu catalysts supported on  $\text{Al}_2\text{O}_3$ ,  $\text{AlSi}_2\text{O}$  and  $\text{SiO}_2$ . *Appl. Catal. B* **2016**, *181*, 24–33. [[CrossRef](#)]
5. Lu, H.F.; Zhou, Y.; Han, W.F.; Huang, H.F.; Chen, Y.F. High thermal stability of ceria based mixed oxide catalysts supported on  $\text{ZrO}_2$  for toluene combustion. *Catal. Sci. Technol.* **2013**, *3*, 1480. [[CrossRef](#)]
6. Ezzatahmedi, N.; Bao, T.; Liu, H.M.; Millar, G.J.; Ayoko, G.A.; Zhu, J.X.; Zhu, R.L.; Liang, X.L.; He, H.P.; Xi, Y.F. Catalytic degradation of orange II in aqueous solution using diatomite-supported bimetallic Fe/Ni nanoparticles. *RSC Adv.* **2018**, *8*, 7687–7696. [[CrossRef](#)]

7. Zhang, Z.H.; Wang, Z.Y. Diatomite-supported Pd nanoparticles: An efficient catalyst for Heck and Suzuki reactions. *J. Org. Chem.* **2006**, *71*, 7485–7487. [[CrossRef](#)]
8. Wang, K.; Tang, Z.H.; Wu, W.; Xi, P.X.; Liu, D.; Ding, Z.Q.; Chen, X.N.; Wu, X.; Chen, S.W. Nanocomposites CoPt-*x*/diatomite-C as oxygen reversible electrocatalysts for zinc-air batteries: Diatomite boosted the catalytic activity and durability. *Electrochim. Acta* **2018**, *284*, 119–127. [[CrossRef](#)]
9. Zhang, G.; Sun, Z.; Duan, Y.; Ma, R.; Zheng, S. Synthesis of nano-TiO<sub>2</sub>/diatomite composite and its photocatalytic degradation of gaseous formaldehyde. *Appl. Surf. Sci.* **2017**, *412*, 105–112. [[CrossRef](#)]
10. Wang, B.; Zhang, G.X.; Leng, X.; Sun, Z.M.; Zheng, S.L. Characterization and improved solar light activity of vanadium doped TiO<sub>2</sub>/diatomite hybrid catalysts. *J. Hazard. Mater.* **2015**, *285*, 212–220. [[CrossRef](#)]
11. Zhou, Y.; Xi, W.; Xie, Z.X.; You, Z.X.; Jiang, X.Z.; Han, B.; Lang, R.; Wu, C.D. High-loading Pt single-atom catalyst on CeO<sub>2</sub>-modified diatomite support. *Chem. Asian J.* **2021**, *16*, 2622–2625. [[CrossRef](#)]
12. Liu, X.; He, Y.; Yang, B.; Qi, Y.; Yang, J. Highly efficient photo-degradation of gaseous organic pollutants catalyzed by diatomite-supported titanium dioxide. *Catalysts* **2020**, *10*, 380. [[CrossRef](#)]
13. Lee, Y.J.; Vikrant, K.; Szulejko, J.E.; Kim, K.H.; Dong, F. Thermocatalytic oxidation of a three-component mixture of volatile organic compounds by a titanium dioxide-supported platinum catalyst. *J. Clean. Prod.* **2021**, *325*, 129279. [[CrossRef](#)]
14. Santos, V.P.; Pereira, M.F.R.; Órfão, J.J.M.; Figueiredo, J.L. Mixture effects during the oxidation of toluene, ethyl acetate and ethanol over a cryptomelane catalyst. *J. Hazard. Mater.* **2011**, *185*, 1236–1240. [[CrossRef](#)]
15. Hou, Z.Y.; Feng, J.; Lin, T.; Zhang, H.L.; Zhou, X.Y.; Chen, Y.Q. The performance of manganese-based catalysts with Ce<sub>0.65</sub>Zr<sub>0.35</sub>O<sub>2</sub> as support for catalytic oxidation of toluene. *Appl. Surf. Sci.* **2018**, *434*, 82–90. [[CrossRef](#)]
16. Ahn, C.W.; You, Y.W.; Heo, I.; Hong, J.S.; Jeon, J.K.; Ko, Y.D.; Kim, Y.; Park, H.; Suh, J.K. Catalytic combustion of volatile organic compound over spherical-shaped copper-manganese oxide. *J. Ind. Eng. Chem.* **2017**, *47*, 439–445. [[CrossRef](#)]
17. Liu, P.; Wei, G.L.; Liang, X.L.; Chen, D.; He, H.P.; Chen, T.H.; Xi, Y.F.; Chen, H.L.; Han, D.H.; Zhu, J.X. Synergetic effect of Cu and Mn oxides supported on palygorskite for the catalytic oxidation of formaldehyde: Dispersion, microstructure, and catalytic performance. *Appl. Clay Sci.* **2018**, *161*, 265–273. [[CrossRef](#)]
18. Chen, J.; Chen, X.; Xu, W.; Xu, Z.; Chen, J.; Jia, H.; Chen, J. Hydrolysis driving redox reaction to synthesize Mn-Fe binary oxides as highly active catalysts for the removal of toluene. *Chem. Eng. J.* **2017**, *330*, 281–293. [[CrossRef](#)]
19. Liu, G.; Yu, J.; Chen, L.; Feng, N.; Meng, J.; Fang, F.; Zhao, P.; Wang, L.; Wan, H.; Guan, G. Promoting diesel soot combustion efficiency over hierarchical brushlike α-MnO<sub>2</sub> and Co<sub>3</sub>O<sub>4</sub> nanoarrays by improving reaction sites. *Ind. Eng. Chem. Res.* **2019**, *58*, 13935–13949. [[CrossRef](#)]
20. Tseng, T.K.; Chu, H.; Hsu, H.H. Characterization of γ-alumina-supported manganese oxide as an incineration catalyst for trichloroethylene. *Environ. Sci. Technol.* **2003**, *37*, 171–176. [[CrossRef](#)]
21. Zhang, D.S.; Zhang, L.; Shi, L.Y.; Fang, C.; Li, H.R.; Gao, R.H.; Huang, L.; Zhang, J.P. In situ supported MnO<sub>x</sub>-CeO<sub>x</sub> on carbon nanotubes for the low-temperature selective catalytic reduction of NO with NH<sub>3</sub>. *Nanoscale* **2013**, *5*, 1127–1136. [[CrossRef](#)] [[PubMed](#)]
22. Baumer, M.; Freund, H.J. Metal deposits on well-ordered oxide films. *Prog. Surf. Sci.* **1999**, *61*, 127–198. [[CrossRef](#)]
23. He, Y.B.; Li, G.R.; Wang, Z.L.; Ou, Y.N.; Tong, Y.X. Pt nanorods aggregates with enhanced electrocatalytic activity toward methanol oxidation. *J. Phys. Chem. C* **2010**, *114*, 19175–19181. [[CrossRef](#)]
24. Prabhuram, J.; Zhao, T.S.; Wong, C.W.; Guo, J.W. Synthesis and physical/electro-chemical characterization of Pt/C nanocatalyst for polymer electrolyte fuel cells. *J. Power Sources* **2004**, *134*, 1–6. [[CrossRef](#)]
25. Cheng, X.; Li, Y.H.; Zheng, L.R.; Yan, Y.; Zhang, Y.F.; Chen, G.; Sun, S.R.; Zhang, J.J. Highly active, stable oxidized platinum clusters as electrocatalysts for the hydrogen evolution reaction. *Energy Environ. Sci.* **2017**, *10*, 2450–2458. [[CrossRef](#)]
26. Priolkar, K.R.; Bera, P.; Sarode, P.R.; Hegde, M.S.; Emura, S.; Kumashiro, R.; Lalla, N.P. Formation of CePdO solid solution in combustion-synthesized Pd/CeO<sub>2</sub> catalyst: XRD, XPS, and EXAFS investigation. *Chem. Mater.* **2002**, *14*, 2120–2128. [[CrossRef](#)]
27. Weng, X.L.; Sun, P.F.; Long, Y.; Meng, Q.J.; Wu, Z.B. Catalytic oxidation of chlorobenzene over Mn<sub>x</sub>Ce<sub>1-x</sub>O<sub>2</sub>/HZSM-5 catalysts: A study with practical implications. *Environ. Sci. Technol.* **2017**, *51*, 8057–8066. [[CrossRef](#)]
28. Pei, W.B.; Liu, Y.X.; Deng, J.G.; Zhang, K.F.; Hou, Z.Q.; Zhao, X.T.; Dai, H.X. Partially embedding Pt nanoparticles in the skeleton of 3DOM Mn<sub>2</sub>O<sub>3</sub>: An effective strategy for enhancing catalytic stability in toluene combustion. *Appl. Catal. B* **2019**, *256*, 117814. [[CrossRef](#)]
29. Zhang, L.; Zou, W.; Ma, K.; Cao, Y.; Xiong, Y.; Wu, S.; Tang, C.; Gao, F.; Dong, L. Sulfated temperature effects on the catalytic activity of CeO<sub>2</sub> in NH<sub>3</sub>-selective catalytic reduction conditions. *J. Phys. Chem. C* **2015**, *119*, 1155–1163. [[CrossRef](#)]
30. Ji, J.; Jing, M.; Wang, X.; Tan, W.; Guo, K.; Li, L.; Wang, X.; Song, W.; Cheng, L.; Sun, J. Activating low-temperature NH<sub>3</sub>-SCR catalyst by breaking the strong interface between acid and redox sites: A case of model Ce<sub>2</sub>(SO<sub>4</sub>)<sub>3</sub>-CeO<sub>2</sub> study. *J. Catal.* **2021**, *399*, 212–223. [[CrossRef](#)]
31. Shan, R.T.; Sheng, Z.T.; Hu, S.; Xiao, H.F.; Zhang, Y.H.; Zhang, J.H.; Wang, L.; Zhang, C.B.; Li, J.L. Enhancing oxidation reaction over Pt-MnO<sub>2</sub> catalyst by activation of surface oxygen. *J. Environ. Sci.* **2023**, in press. [[CrossRef](#)]
32. Murugan, B.; Ramaswamy, A.V.; Srinivas, D.; Gopinath, C.S.; Ramaswamy, V. Nature of manganese species in Ce<sub>1-x</sub>Mn<sub>x</sub>O<sub>2-δ</sub> solid solutions synthesized by the solution combustion route. *Chem. Mater.* **2005**, *17*, 3983–3993. [[CrossRef](#)]
33. Zhao, H.J.; Dong, F.; Han, W.L.; Tang, Z.C. Study of morphology-dependent and crystal-plane effects of CeMnO<sub>x</sub> catalysts for 1,2-dichlorobenzene catalytic elimination. *Ind. Eng. Chem. Res.* **2019**, *58*, 18055–18064. [[CrossRef](#)]
34. Tang, W.X.; Wu, X.F.; Li, D.Y.; Wang, Z.; Liu, G.; Liu, H.D.; Chen, Y.F. Oxalate route for promoting activity of manganese oxide catalysts in total VOCs' oxidation: Effect of calcination temperature and preparation method. *J. Mater. Chem. A* **2014**, *2*, 2544–2554. [[CrossRef](#)]

35. Hao, X.Q.; Deng, J.G.; Liu, Y.X.; Jing, L.; Wang, J.; Wang, Z.W.; Dai, H.X. Mesoporous  $\text{Na}_x\text{MnO}_y$ -supported platinum–cobalt bimetallic single-atom catalysts with good sulfur dioxide tolerance in propane oxidation. *ACS Sustain. Chem. Eng.* **2022**, *10*, 8326–8341. [[CrossRef](#)]
36. Kim, S.C.; Shim, W.G. Catalytic combustion of VOCs over a series of manganese oxide catalysts. *Appl. Catal. B* **2010**, *98*, 180–185. [[CrossRef](#)]
37. Du, H.; Wang, Y.; Arandiyani, H.; Younis, A.; Scott, J.; Qu, B.; Wan, T.; Lin, X.; Chen, J.; Chu, D. Design and synthesis of  $\text{CeO}_2$  nanowire/ $\text{MnO}_2$  nanosheet heterogeneous structure for enhanced catalytic properties. *Mater. Today Commun.* **2017**, *11*, 103–111. [[CrossRef](#)]
38. Li, P.; He, C.; Cheng, J.; Ma, C.Y.; Dou, B.J.; Hao, Z.P. Catalytic oxidation of toluene over Pd/ $\text{Co}_3\text{AlO}$  catalysts derived from hydrotalcite-like compounds: Effects of preparation methods. *Appl. Catal. B* **2011**, *101*, 570–579. [[CrossRef](#)]
39. Zhao, S.; Hu, F.Y.; Li, J.H. Hierarchical core-shell  $\text{Al}_2\text{O}_3$ @Pd–CoAlO microspheres for low-temperature toluene combustion. *ACS Catal.* **2016**, *6*, 3433–3441. [[CrossRef](#)]
40. Liao, Y.N.; Zhang, X.N.; Peng, R.S.; Zhao, M.Q.; Ye, D.Q. Catalytic properties of manganese oxide polyhedra with hollow and solid morphologies in toluene removal. *Appl. Surf. Sci.* **2017**, *405*, 20–28. [[CrossRef](#)]
41. Li, J.; Na, H.; Zeng, X.; Zhu, T.; Liu, Z. In situ DRIFTS investigation for the oxidation of toluene by ozone over Mn/HZSM-5, Ag/HZSM-5 and Mn–Ag/HZSM-5 catalysts. *Appl. Surf. Sci.* **2014**, *311*, 690–696. [[CrossRef](#)]
42. Zhang, X.; Dai, L.Y.; Liu, Y.X.; Deng, J.G.; Jing, L.; Wang, Z.W.; Pei, W.B.; Yu, X.H.; Wang, J.; Dai, H.X. Effect of support nature on catalytic activity of the bimetallic RuCo nanoparticles for the oxidative removal of 1,2-dichloroethane. *Appl. Catal. B* **2021**, *285*, 119804. [[CrossRef](#)]
43. Bai, S.X.; Dai, Q.G.; Chu, X.X.; Wang, X.Y. Dehydrochlorination of 1,2-dichloroethane over Ba-modified  $\text{Al}_2\text{O}_3$  catalysts. *RSC Adv.* **2016**, *6*, 52564–52574. [[CrossRef](#)]
44. Liu, X.L.; Han, Q.Z.; Shi, W.B.; Zhang, C.; Li, E.; Zhu, T.Y. Catalytic oxidation of ethyl acetate over Ru–Cu bimetallic catalysts: Further insights into reaction mechanism via in situ FTIR and DFT studies. *J. Catal.* **2019**, *369*, 482–492. [[CrossRef](#)]
45. Rainone, F.; Bulushev, D.A.; Kiwi-Minsker, L.; Renken, A. DRIFTS and transient-response study of vanadia/titania catalysts during toluene partial oxidation. *Phys. Chem. Chem. Phys.* **2003**, *5*, 4445–4449. [[CrossRef](#)]
46. Naydenov, A.; Velinova, R.; Blin, J.-L.; Michelin, L.; Lebeau, B.; Kolev, H.; Karakirova, Y.; Karashanova, D.; Vidal, L.; Dotzeva, A.; et al. Reaction kinetics and mechanism of VOCs combustion on Mn–Ce–SBA-15. *Catalysts* **2022**, *12*, 583. [[CrossRef](#)]
47. Behar, S.; Gómez-Mendoza, N.A.; Gómez-García, M.A.; Swierczynski, D.; Quignard, F.; Tanchoux, N. Study and modelling of kinetics of the oxidation of VOC catalyzed by nanosized Cu–Mn spinels prepared via an alginate route. *Appl. Catal. A* **2015**, *504*, 203–210. [[CrossRef](#)]
48. Chen, B.; Bai, C.; Cook, R.; Wright, J.; Wang, C. Gold/cobalt oxide catalysts for oxidative destruction of dichloromethane. *Catal. Today* **1996**, *30*, 15–20. [[CrossRef](#)]
49. Xie, S.H.; Liu, Y.X.; Deng, J.G.; Yang, J.; Zhao, X.T.; Han, Z.; Zhang, K.F.; Wang, Y.; Arandiyani, H.; Dai, H.X. Mesoporous CoO-supported palladium nanocatalysts with high performance for *o*-xylene combustion. *Catal. Sci. Technol.* **2018**, *8*, 806–816. [[CrossRef](#)]
50. Wu, L.K.; Deng, J.G.; Liu, Y.X.; Jing, L.; Yu, X.H.; Zhang, X.; Gao, R.Y.; Pei, W.B.; Hao, X.Q.; Rastegarpanah, A.; et al. Pd/silicalite-1: Pd/silicalite-1: An highly active catalyst for the oxidative removal of toluene. *J. Environ. Sci.* **2022**, *116*, 209–219. [[CrossRef](#)]
51. Niu, L.J.; Xian, G.; Long, Z.Q.; Zhang, G.M.; Zhou, N.Y.  $\text{MnCeO}_x$ /diatomite catalyst for persulfate activation to degrade organic pollutants. *J. Environ. Sci.* **2020**, *89*, 206–217. [[CrossRef](#)]
52. Liu, P.; He, P.; Wei, G.L.; Liu, D.; Liang, X.L.; Chen, T.H.; Zhu, J.X.; Zhu, R.L. An efficient catalyst of manganese supported on diatomite for toluene oxidation: Manganese species, catalytic performance, and structure activity relationship. *Microporous Mesoporous Mater.* **2017**, *239*, 101–110. [[CrossRef](#)]
53. Jiang, Y.; Gao, J.; Zhang, Q.; Liu, Z.; Fu, M.; Wu, J.; Hu, Y.; Ye, D. Enhanced oxygen vacancies to improve ethyl acetate oxidation over  $\text{MnO}_x$ – $\text{CeO}_2$  catalyst derived from MOF template. *Chem. Eng. J.* **2019**, *371*, 78–87. [[CrossRef](#)]
54. Li, Q.; Zhai, Z.; Xu, Y.; Jia, L.S.; Huang, J.L.; Sun, D.H.; Li, Q.B. Diatomite supported Pt nanoparticles as efficient catalyst for benzene removal. *Ind. Eng. Chem. Res.* **2019**, *58*, 14008–14015. [[CrossRef](#)]
55. He, C.; Li, P.; Cheng, J.; Hao, Z.P.; Xu, Z.P. A Comprehensive study of deep catalytic oxidation of benzene, toluene, ethyl acetate, and their mixtures over Pd/ZSM-5 catalyst: Mutual effects and kinetics. *Water Air Soil Pollut.* **2010**, *209*, 365–376. [[CrossRef](#)]
56. Dong, N.; Chen, M.Y.; Ye, Q.; Zhang, D.; Dai, H.X. An investigation on catalytic performance and reaction mechanisms of Fe/OMS-2 for the oxidation of carbon monoxide, ethyl acetate, and toluene. *J. Environ. Sci.* **2022**, *112*, 258–268. [[CrossRef](#)]
57. Saper, S.M.; Kondarides, D.I.; Verykios, X.E. Catalytic oxidation of toluene over binary mixtures of copper, manganese and cerium oxides supported on  $\gamma$ - $\text{Al}_2\text{O}_3$ . *Appl. Catal. B* **2011**, *103*, 275–286.
58. Su, X.W.; Jin, L.Y.; Lu, Q.; Luo, M.F. Pd/ $\text{Ce}_{0.9}\text{Cu}_{0.1}\text{O}_{1.9}$ – $\text{Y}_2\text{O}_3$  catalysts for catalytic combustion of toluene and ethyl acetate. *J. Ind. Eng. Chem.* **2009**, *15*, 683–686. [[CrossRef](#)]
59. Beauchet, R.; Magnoux, P.; Mijoin, J. Catalytic oxidation of volatile organic compounds (VOCs) mixture (isopropanol/*o*-xylene) on zeolite catalysts. *Catal. Today* **2007**, *124*, 118–123. [[CrossRef](#)]

**Disclaimer/Publisher’s Note:** The statements, opinions and data contained in all publications are solely those of the individual author(s) and contributor(s) and not of MDPI and/or the editor(s). MDPI and/or the editor(s) disclaim responsibility for any injury to people or property resulting from any ideas, methods, instructions or products referred to in the content.